Fermi National Accelerator Laboratory

FERMILAB-Pub-87/173-E
[E-741/CDF]

CDF End Plug Electromagnetic Calorimeter Using Conductive Plastic Proportional Tubes*

Y. Fukui, M. Mishina
National Laboratory for High Energy Physics, KEK
Oho-machi, Tsukuba-gun, Ibaraki-ken, 305, Japan

Y. Hayashide, S. Kanda, S. Kim, K. Kondo, S. Miyashita, H. Miyata.
Y. Morita, M. Shibata, K. Takikawa
Institute of Physics, University of Tsukuba
Niihari-gun, Ibaraki-ken, 305, Japan

S. Mori
Faculty of Engineering Science, University of Tsukuba
Niihari-gun, Ibaraki-ken, 305, Japan

Y. Muraki
Institute for Cosmic Ray Research, Tokyo University
Midori-cho, Tanashi-shi, Tokyo, 188, Japan

July-August 1987

*Submitted to Nucl. Instrum. Methods A

CDF END PLUG ELECTROMAGNETIC CALORIMETER USING CONDUCTIVE PLASTIC PROPORTIONAL TUBES

Y.Fukui, M.Mishina
National Laboratory for High Energy Physics, KEK
Oho-machi, Tsukuba-gun, Ibaraki-ken, 305, Japan

Y.Hayashide, S.Kanda, S.Kim, K.Kondo, S.Miyashita, H.Miyata,
Y.Morita, M.Shibata, K.Takikawa
Institute of Physics, University of Tsukuba
Niihari-gun, Ibaraki-ken, 305, Japan

S. Mori
Faculty of Engineering Science , University of Tsukuba
Niihari-gun, Ibaraki-ken, 305, Japan

Y.Muraki
Institute for Cosmic Ray Research, Tokyo University
Midori-cho, Tanashi-shi, Tokyo, 188, Japan

A 2.8 *m* diameter and 50 *cm* deep round disc shaped calorimeter has been built for each of the forward and the backward opening of the central detector structure of the Collider Detector at Fermilab (CDF) using conductive plastic proportioal tube arrays sandwiched with lead absorber panels. A thorough use of cathode read-out based on pads and strips etched on the printed circuit boards on the chambers enabled us to construct a finely segmented projective tower geometry defined by a polar coodinate system with the origin at the center of the detector with minimal dead region. These modules were tested for various properties with high energy electron beams and completely mapped with 100 *GeV* electron beams. The response map was then used as the input for a χ^2-minimization procedure and an improved uniformity of 1.3 % in r.m.s. was obtained. A factor of 500 to 1000 rejection of pions was obtained using correlation matrix without relying on momentum measurement.

1. GEOMETRY

The end plug electromagnetic calorimeter covers both ends of the 3-meter diameter 5-meter long solenoid in the central detector system of CDF leaving a concentric conical hole of an opening angle of 10° with respect to the beam axis in either direction. Each of the two calorimeter modules occupies a cylindrical volume of an outer diameter of 280 *cm* and a depth of 53 *cm* between 173 *cm* and 226 *cm* in z –coordinate along the beam axis. The angular coverage is from 10° to about 36° in the polar angle θ, or in the pseudorapidity η from about 1.1 to 2.4, with full depth up to 32°. Such geometry is shown in Fig. 1 as a cross sectional view of the end plug region of CDF central detector structure.

2. DESIGN CRITERIA

The conditions and the basic requirements which were the basis for the choice of the design were as follows:

1) Geometrical constraints ---a) Cylindrical outer shape and conical hole of θ= 10°.
   b) Large system of 280 *cm* in outer diameter.
   c) Desirable projective tower defined by polar coordinates.
   d) Limited available depth of about 50 *cm* along z.
2) Strong, 15 *kGauss*, solenoidal magnetic field.
3) Fine lateral segmentation to measure the energy flow as a function of (η , ϕ) coordinates.
4) Limited accuracy in momentum measurement of the charged tracks in this region because the tracks exit the central tracking chamber through the end plate without traversing all the wire layers.

   ....At least three segments in depth to measure the longitudinal shower profile to help identify electrons.
5) Good hermeticity.
6) Reasonably good energy resolution.

A fine segmentation is essential for isolating electron signals which are important signatures of interesting events. It is also a necessary tool to identify jets with their masses.

It was judged that a scintillator system is not appropriate in this region. Any type of light guides to lead the light to the outside of the magnetic field inevitably introduces a substantial dead/hot region if one tries to make a fine lateral segmentaion and/or more than one longitudinal segments. In this angular region, it is also difficult to make a reasonably well defined projective tower by scintillators.

All of these considerations pointed towards a proportional chamber based system. If the signals are read out from cathode pads and strips, patterns of any shape and size can be implemented virtually without any dead space. The longitudinal segmentation is also simply a matter of cabling.

In order to maintain the gap height of the chamber over a large surface area, a proportional tube arrays, instead of parallel plate chamber, were conceived. Proportional tube arrays are preferred also because it reduces the solid angle for secondary δ-rays to traverse in the gas which cause fluctuations both in the energy deposit and in the shower profile.

Since the tube orientaion is perpendicular to the solenoidal magnetic field, the effect of the magnetic field on the secondary electron tracks was presumed to be small.

With proportional tubes of reasonably small profile, one can stack an enough total thickness into the allocated depth.

With minimizing the boundaries of the proportional tube arrays, a good hermeticity can be achieved.

Choice of proportional tubes as the sensing media is not necessarily a compromise in the energy resolution because the laboratory momentum of the particles of any given transverse momentum Pt has a boost due to the factor $1/\sin\theta$ which ranges from 2 to 5.5 in this angular region. Therefore based on an empirical formula of energy resolution of gas calorimeter

$$\sigma_E / E = 30\% \sqrt{t / E} \qquad (1)$$

where t is the thickness of each layer in radiation length, the energy resolution for a given Pt is expected to be essentially comparable to the scintillator calorimeter in the central region of CDF.

After these considerations it was decided to build the calorimeter with proportional tubes made out of conductive plastic tubes interleaved with lead absorber panels. High resistivity of the conductive plastic tubes enables to pick up the avalanche-induced signals by pads and strips etched on printed circuit boards which sandwitch the tube array on each of the chamber layers .

The patterns of the pads and the strips are defined by polar coordinate η, ϕ, and z in order to form well segmented projective towers. Longitudinally each pad tower is segmented into three parts, the first and the last being shallow and the middle being deep in order to contain most of the electromagnetic shower energies.

It was decided to implement strips of four to five times finer steps for the layers around the shower maximum to be able to examine a finer structure of the shower core of more or less isolated electron candidate events to see whether the shower is truely from one particle. This was conceived to help reject copious background from π^0's, or low energy electrons or γ's overlapped with high momentum hadrons.

3. CHAMBER STRUCTURE

Each of the modules consists of four quadrants of $\Delta\phi = 90^\circ$ each, and each of the quadrants consists of 34 layers of proportional tube arrays interleaved with 2.7 *mm* thick lead absorber panels filling about 50 *cm* in depth in *z* direction. An exploded view of such a layer is sketched in Fig.2 .

The lead panels were made of lead alloy with 0.065 % calcium and 0.7 % tin which had a factor of 2 larger ultimate tensile strength and four times smaller elongation than ordinary 6 % antimony loaded lead [(1)].

The proportional tubes were made of conductive plastic tubes of a square inner cross section of 7 *mm* x 7 *mm* with 0.8 *mm* thick wall and anode wires of 50 μm gold plated tungsten supported by Y-shaped molded plastic pieces at both ends, as skeched in Fig. 3. The conductive plastic tubes were extruded out of polystyrene loaded with fine grain carbon powder [(2)]. The surface resistance was chosen to be in a range of 60 to 100 $k\Omega$ / *square* . Since the gain of a proportional tube is quite sensitive to the physical dimensions of the components [(3)], the tolerance of the inner dimension was kept within $\pm$ 100 μm . The wall thickness was maintained within $\pm$ 50 μm . The tolerance of the anode wire diameter was specified to $\pm$ 0.5% and the plastic molding for the wire support was specified to $\pm$ 100 μm in the dimensional tolerance of the position of the saddle point. The wire tension was about 150 *gr* .

Each plane of the tube arrays was assembled into a fan-shaped quadrant in azimuth in which all 156 tubes were vertical or horizontal in a plane perpendicular to the beam axis, but were trimmed tube by tube to form a circular arc of $\Delta\phi = 90^\circ$ at the inner conical wall of $\theta = 10^\circ$ and the outer cylindrical boundary. Due to tube to tube steps and recesses around supporting rods at every 15° at $r = 136$ *cm* , guaranteed 100 % sensitivity circle lies at about $r = 131$ *cm* taking account of the sensitivity decrease in a region within 1 *cm* from the tube end. 80 % of the circumference is 100 % sensitive at 133 *cm* and 136 *cm* is the real edge. At the inner circumference , due to the similar situation including the necessary recesses for the gas manifold at every 30°, as discussed later, 100 % sensitivity is guaranteed at about 3 *cm* from the 10°-cone corresponding to $\theta = 11^\circ$. At 10.5°, 80 % of the circumference is 100 % sensitive.

Since the tube arrays were pushed against one of the orthogonal straight edges parallel to the tubes, there was virtually no dead space along that edge, while along the other straight edge orthogonal to the tube orientation there were about 5 *mm* wide dead zone for terminating the anode wires and another several *mm* wide zone of reduced sensitivity inherent to an end of a proportional tube. However by rotating the orientation of the tubes by 90° layer by layer real dead zone is only the physical gap between contiguous quadrants which were kept to within 3 *mm* . The tube arrays were sandwitched by a pair of 1.6 *mm* thick G-10 panels with structural adhesive. Since the gain of the proportional tubes is sensitive to the anode wire displacement from the center of the tube [(3),(4)], a great caution was taken to keep the tubes straight within the chamber plane when the tube panels were assembled.

Material thickness of each layer is listed in Table 1. The total material thickness varies inversely proportional to $cos\theta$ up to 30° and then decreases rapidly due to the fact that the particle track penetrates to the cylindrical outer periphery.

The pads were etched out of the copper plating clad on G-10 panels on one side of every proportional tube panels directly facing to the tube array, segmented with boundaries defined by polar coordinates η, ϕ, and z. In the polar angle the segmentation was $\Delta\eta = 0.09$ between 1.41 and 2.4 in η, and smaller for larger angles. In the azimuthal angle the step was 5°. The pattern of the pads is shown in Fig.4 *a*. All the pads were flared in size with increasing z according to the definition. Longitudinally these pads were ganged together at each of the polar coordinate (η, θ) into three projective towers. The first segment contains the first five layers, the second the next twenty four, and the third the last five, respectively. An isometric view of a quadrant module showing the pattern of the pads and the side view of such projective towers is sketched in Fig.5.

Besides the pads, the first ten layers of the second longitudinal segment, 6-th through 15-th layers, have strips of two types on the rear side G-10 panels. They are orthogonal with each other with patterns illustrated in Figs. 4 *b* and 4 *c*. Odd-numbered five layers have θ–strips which are 32 arc shaped strips of $\Delta\eta = 0.02$ stretched by 30° in ϕ, and the rest five even numbered layers have ϕ–strips which are thirty radial strips of $\Delta\phi = 1°$. The coverage of these strips in polar angle is limited to a region of $\eta = 1.2$ to 1.84. It was based on a judgement that any larger θ region is not much worth of implementing strips because of inferior energy measurement due to the leakage at the boundary. The smaller θ region is already well segmented by the pads. All five θ–strips are ganged together in depth at the same (η , ϕ) coordinate also forming well defined projective towers, and so are the ϕ-strips independently. In Table 2 the total number of signals is listed. Also Table 3 summarizes the chamber layer configuration.

On each of the G-10 boards, signals from the pads and the strips are brought radially to the outer circular edge of the board by etched strip lines and connected to edge card connectors. One 34-pin connector at every 5° in ϕ collects signals from sixteen pads in the radial row at the corresponding ϕ and two 34-pin connectors per 30° are assigned to each of θ– and ϕ–strips within the corresponding $\Delta\phi = 30°$ sector. The longitudinal segmentation was achieved by simply ganging the necessary number of connectors at the same ϕ by a flat ribbon cable.

The anode wires were bussed together in each of the quadrant panels through a 100 Ω resistor on individual wire. The signals were each picked off a 50 Ω coaxial cable which feeds high voltage to each quadrant panel.

4. MECHANICAL STRUCTURE

The entire stack of each module is contained in a gas tight vessel for each of the forward and the backward end plugs. An isometric view of the vessel is shown in Fig.6 .

Each of the gas vessels consists of a 4.45 *cm* thick round rear plate, a round 1.27 *cm* thick front cover plate, a conical wall at the inner circumference at $\theta = 10^\circ$, and a cylindrical wall around the outer circumference . The cylindrical wall around the outer circumference is divided into 30° sections in ϕ and each section has a curved window frame, which is mostly milled out, and a curved cover plate.

At every 15° in ϕ and close to the outer circumference in radius,there are twenty four rods, 3 *cm* in diameter, supported by the bottom and the front plates, forming a "Ferris wheel" like cage. In each quadrant volume, the proportional tube panels and interleaving lead panels were glued together in depth making eight rigid blocks, the first six blocks being with four layers each and the rest two blocks with five layers each . The process of glueing was done cautiously in order to assure the flatness of the tube panels . Every block was kept pressed against a flat steel bed ,whose surface
was ground to better than 50 μm , for minimum of 24 hours with 1 *atm* pressure at curing time of the glue. Flatness of the surface of every block was measured to be within ±100 μm. These blocks were then hung on the supporting rods at the corresponding holes close to the outer circumference. The gas vessel is supported vertically in front of the end plug hadron calorimeter by steel bars horizontally extended from the hadron calorimeter structure at every 15 ° in ϕ around the outer circumference and around the inner $\theta = 10^\circ$ cone.

With removing the cover plates on the outer circumference, most part of the side of the calorimeter stack and the signal and the high voltage feed-through boards are accessible for checking after all the calorimeter layers are stacked and mechanically fastened to the vessel.

The materials are all non-magnetic except for the rear steel plate which is a part of the flux return end plug structure for the solenoidal magnetic field. All of the structural members, the $\theta = 10^\circ$ conical wall, the supporting rods, the window frames, and the 1.27 *cm* front cover plate, are made of stainless steel and the cylindrical side covers are made of aluminum.

The penetration of the pad and strip signals and the high voltage through the gas vessel was made by feed-through boards mounted in small enclosures at the rear corner around the outer circumference . These feed-through boards are distributed around the outer circumference so that all the signal cables find their feed-through board at the same ϕ without any detouring. Since these enclosures are at the farthest corner from the interaction point, there is enough thickness of more than 18 radiation length in front of the enclosure.

The parameters of the module is summarized in Table 4 .

5. GAS SYSTEM

Every other supporting rod is hollowed and has 34 small holes each at a position corresponding to every chamber layer facing towards the chamber. These twelve rods are used as gas manifolds with gas being fed at the end where the rods are welded into the rear steel plate. There are also hollowed rectangular columns with small holes at every 30° in ϕ on the inner conical wall of $\theta = 10°$ as outlet manifolds. All the inlets of a vessel are fed with gas parallely and the outlets are also connected to the exhaust line in parallel, as sketched in Fig.7 .

The empty volume of about 1.2 m^3 of each of the vessels was kept replaced by gas with a slow flow rate, about 100 *cc / min*, to compensate a minor leakage of about 50 *cc /min*.

Argon-ethane of 50 % - 50 % mixture with small percentage of ethyl alcohol admixture has been exclusively used throughout the test and the calibration runs. This gas mixture has been extensively tested [5] and has shown excellent properties against aging problems. Alcohol mixture prevents a continuous glow discharge to develop when a large dose of radiation shines a small spot. Since a recent study [6] has shown that isopropyl alcohol is superior as such a quenching agent, it is used in the final CDF detector instead of ethyl alcohol. This change of the alcohol admixture does not create a problem in maintaining the calibration of the absolute energy scale beacuse the energy scale is solely maintained by the signals from radioactive sources embedded within the same gas environment as is discussed later.

Alcohol percentage is regulated by feeding the inlet gas through a bubbler immersed in alkohol in a refrigerating bath whose temperature is kept within ±0.1°*C* around -3°*C* .

6. ELECTRICAL CHARACTERISTICS AND READ OUT

The area of the pads ranges from about 3 *cm* x 3 *cm* to 10 *cm* x 19 *cm* in the first layer depending on η , and flares out by up to 30 % with increasing z, comprising a sizable capacitance with the wall of the conductive plastic tubes. The measured capacitances of the pad towers were consistent with the values calculated with the following parallel plate formula

$$C = 8.855 \cdot \varepsilon \cdot S / d \quad (pF) \qquad (2)$$

where S is the total area of the pads in m^2 and d is the distance in m , assuming the dielectric constant ε of 4 and $d = 70\ \mu m$ corresponding to the gap between the pad surface and the conductive plastic tube wall. The largest capacitance comes from the second longitudinal segment of the tower in which 24 pads in depth are ganged together. The maximum value is for the tower at $\theta = 25°$ which was measured to be about 110 *nF*. Based on the measurement made on one of the prototype module [7], the rise time of the shower signal from the anode wire is estimated to be about 70 *n sec* in the present case of 7 *mm* x 7 *mm* tube [8]. The observed exponential fall time of the signal from the pad is a product $R \cdot C$, in which R corresponds to the cable impedance assuming that the input impedance of the read-out electronics is matched with it, and C is the capacitance of the pad tower segment. Therefore custom made 14 Ω ribbon coaxial cables were used to bring the signals from the pads and the strips to the charge amplifier placed on the outside of the end plugs with minimal time constant to drain the signals. The cables were 7 *meter* long each and the input impedance of the charge-integrating amplifier was designed to be about 12 Ω in order to have a reasonable matching. The signal is integrated for 1.6 μ *sec* after the beam crossing and a measurement indicates that more than 95 % of the charge is integrated even for the worst case. It is planned to reduce the time constant further by implementing a low impedance input buffer circuit within the gas vessel in near future.

The charge-integrating amplifier developed for CDF [9] has a front end charge integrator followed by two sample-hold circuits with an analog switch in front of each. Thus the base line sampled at 200 *n sec* before the beam crossing can be subtracted from the charge signal sampled at 1.6 μ *sec* after the beam crossing so that the output is essentially free from slowly changing tail of the preceding signal or low frequency noise. The analog output, maximum of 2.5 *V* for 500 *pC* input ,is scanned by a single 16-bit ADC which is common to all channels, up to 504 channels, in a crate. 24 channels are housed in a CARROT type modules. There is an on-board charge injection pulser which can inject a known amount of charge, stored in a 100 *pF* capacitor by a d.c. voltage given by a 12-bit DAC, into a selected channel at the front end. The gains of all channels are adjusted to ±1 % at the time of the module assembly. The pedestal values, measured on all 8400 channels after the calorimeter modules were installed onto the CDF detector structure and completely cabled, were very stable and the r.m.s. spread of the pedestal was less than 12 L.S.B. counts, or about 0.1 *pC* or less.

7. GAS GAIN MONITORING

Through the beam test on the prototype modules, it had been known that the calorimeter response is quite sensitive to the change in the operational conditions such as the high voltage, the gas temperature, and the gas pressure [3]. Since one cannot presume that the effects are simply additive, the overall gain has to be monitored rather than monitoring the variation of individual parameters.

A test made on a prototype module[3] has demonstrated that, monitoring a peak in the spectrum of low energy X-ray emitting radioactive source mounted on a tube identical to those in the calorimeter stack within the same gas vessel, one can trace the gas gain for high energy electron-induced shower to an accuracy better than a per cent. 5.9 *keV* X-ray from Fe^{55} is appropriate for this purpose since it penetrates the 0.8 *mm* thick wall of the conductive plastic tubes and the converted electrons stop mostly within the 7 *mm* x 7*mm* gas volume forming a sharp peak of a width of about 6 to 8 % in r.m.s.. A 1 μ *Curie* Fe^{55} source deposited on a 50 μ *m* wire, spread over about 2 cm along the wire [10], was glued onto the outside of each of a 10-*cm* long proportional tubes identical to the tubes used in the calorimeter. Fig. 8 is a typical spectrum taken from one of the monitoring tubes installed in the final calorimeter module.

Twenty four such tubes were distributed with regular steps around the outer circumference within the gap between the gas vessel and the calorimeter stack within each of the gas vessels. The outputs were continuously monitored throughout the calibration run which took about two weeks for each of the modules.

Since the charge output of 5.9 *keV* peak of Fe^{55} from such tube is about 0.3 *pC* for 1.9 *kV* operation, a high gain charge-integrating amplifier was developed [9]. The circuitry is similar to the CARROT amplifier in that it is a two-sample system, but it is a self triggering system in which the amplified signal is sent to a LSI-11 driven monitoring system while the integrated signal is delayed by 1.8 μ *sec* to wait for the strobe signal to come back from the trigger logic. The modules, each housing 16 channels, have been tested and have shown excellent properties, such as linearity, stability, and quietness, and have been inplemented to the monitoring tubes. In order to make the 5.9 *keV* peak essentially noise free to ease the fitting process, tubes are operated at 1.9 *kV* although the calorimeter is operated at lower high voltage value, 1.7 *kV*.

Through the first engineering run of CDF, it was demonstrated that such monitoring was in fact quite reliable. Fig.9 shows the plots of signals from 21 monitoring tubes embedded within one of the calorimeter modules for about two month period out of the total of five months of the run. Each data point represents a 5.9 *keV* peak determined from a pulse height spectrum of 1000 events accumulated within about 10 *min*, and the sampling was made at a few to several hour intervals. Each of the signals was normalized by the mean value of all of the tubes and the vertical axis was shifted one by one to distinguish individual behavior. The r.m.s. spread of each of the tubes is about 0.4 % except for one tube of 0.6 % and the r.m.s. spread of all the data is 0.44 % after normalization allocating one constant factor to each of the tubes. This observation confirms that tubes are closely tracking each other and gives a confidence that the gain of the calorimeter against high energy particles is well normalized by these monitoring tube data. An attemt to normalize these data by correcting for the measured temperature and the barometric pressure has failed to give such a precision. The fact that all the tubes distributed around the outer cirrcumference have shown constant relative gain provided an evidence that there was no time dependent local disturbance of the gas conditions within the gas vessel.

8. BEAM TEST RESULTS

After three generations of prototype modules have been built and tested for general characteristics by high energy electron beam at Fermilab up to 200 *GeV* [2],[7],[11], the two final calorimeter modules were built and exposed to the beam for various tests and for the final energy calibration.

8.1 TEST BEAM LINE

The beam was either of purified electron beam or purified negative hadron beam with small fraction of contamination of the undesirable particle species. Particle by particle, the incident beam ray and momentum were measured by a set of analyzing magnets implemented with a set of proportional chambers . The measured momentum resolution was better than 0.5% at and above 100 *GeV* out of overall ± 4 % momentum bite of the beam and the incident point was measured to better than 1 *mm* while 2.5 *cm* x 2.5 *cm* cross sectional area was taken out of a slightly larger beam profile[12].

The calorimeter module was mounted on a fixture which was designed to rotate the module in both vertical and horizontal directions to align any of the pad towers to the incident beam axis. The fixture was computer controlled in such that the module was rotated, after accumulating about 1000 events at every spot, from one angle to the next within a 40 *sec* interval before the subsequent beam spill . The angles were monitored by 14-bit rotary encoders to an accuracy of 0.02°.

8.2 ELECTRON SHOWER PROFILE

Fig.10 shows a typical lego plot of electron induced showers measured by the pad towers and Fig.11 is the longitudinal profile of the showers measured by the anode wire layers. The fractional fluctuation of the layer by layer signal is smallest at the layers around the shower maximum as shown in Fig.12 .

A reasonable fit to the longitudinal profile was obtained by a formula of the following form[13]

$$\Delta E/\Delta t \; = \; A \, t^{\alpha} \, e^{-\beta t} \qquad (3)$$

with parameters A, α , and β of the following energy dependences:

$$A = E \cdot \beta^{\alpha+1} / \, \Gamma(\alpha+1),$$

$$\alpha = a + b \cdot ln\, E\,,$$

and

$$\beta = c + d \cdot ln\, E$$

where a, b, c, and d are constatnts.

8.3 SHOWER LEAKAGE

In Fig.13 the logitudinal shower leakage at θ=20° was plotted against the incident energies at 1.8 *kV* . Data points from 20 to 200 *GeV* were calculated as the difference between the integral to an infinite thickness of a curve fitted to the layer-by-layer signals at the tail of the shower beyond 15 radiation length and the measured signals up to 34 layers. The curves are shown for the different angles using the parametrization derived from the above data.

8.4 ENERGY RESOLUTION

In Fig.14 the energy resolutions of the summed pad signals at 1.8 kV is plotted against a quantity $1/\sqrt{E}$. The resolution is slightly worse than the canonical value based on Eq. (1) which was obtained on the prototype modules. Even though the pads are etched only on one side of every chamber, the energy resolutions are essentially the same as that of the summed anode wire signals in good accuracy.

In order to find an optimum high voltage value, the energy resolution of the pad signals was plotted against the high voltage in Fig.15. The energy resolution becomes worse above 1.85 kV which corresponds to the end of proportional region. Since the energy resolution is not much different down to 1.65 kV, 1.7 kV was chosen as the final operating point in order to avoid gain saturation as discussed below.

8.5 GAIN SATURATION

At higher range of the high voltage values, signal saturation is expected, especially for higher energies. A sensitive way of examining whether any layer is saturated is to make a comparison of the layer-by-layer responses for different voltages. Figs.16 *a* and *b* are the scatter plots for 1.7 kV vs. 1.65 kV and 1.85 kV vs. 1.65 kV, respectively, with 100 GeV electrons. The two-valued correlation seen in Fig.16*b* is indicative of saturation in some of the layers, whereas in Fig.16*a* points are well clustered around a straight line indicating that up to 1.7 kV the chambers are not much saturated for 100 GeV incident electrons. Notice that such a plot is not affected by a possible energy dependent effect such as the leakage from the back of the calorimeter. The trend is further examined in Fig.17 in which the layer-by-layer signals for various voltages are normalized to those for 1.65 kV. All the points are further normalized using the average of the last eight layers which are flat in response indicating there is no appreciable saturation. At the tail of the shower, in addition to the fact that the energy deposit is small, the shower is well spread laterally resulting in much smaller track density than the shallower layers. Severest saturation is seen in the layers in front of the shower maximum where the shower is already developed but is not much spread laterally causing high track density. It is obvious that the choice of 1.7 kV as the operating point is well justified with regard to the saturation.

8.6 LINEARITY

An estimate of nonlinearity of the response against the incident energy was made for various incident energies. In Fig.18 data points for 1.8 kV were fitted by a quadratic form. The quadratic term becomes about 16 % at 200 GeV out of which 4 % is accounted for by the longitudinal leakage as discussed before. At 1.7 kV, which was the operating point, the nonlinearity is much less significant.

8.7 POSITION MEASUREMENT

Using the tower by tower energy deposits the centroid of the shower was calculated as the first moment. Figs.19 *a* and *b* are the scatter plots of the shower centroid in radial direction thus calculated from the energy deposits in the second longitudinal segments and in the θ-strips, respectively, against the angle of the rotating fixture. Minute ripple in the plot for the pads is due to the finite size of the pads and the simplified algorithm in which the center of the pads are taken as the coordinate of the pads. The angle measurement by the θ-strips ends at near to 18° below which the strips are not implemented. Figs.20 *a* and *b* are the r.m.s. error in such position determination using the signals from the second longitudinal segments of the pad towers. *a* is the plot of the resolution in θ-direction and *b* is the resolution in ϕ-direction , both in degree. The resolution in ϕ-direction is 0.2° to 0.3° and flat in terms of the angle with varying θ . The resolution in θ-direction is about 0.04° to 0.2°. The angular resolutions measured by the strips are 0.04° to 0.06° in θ-direction by θ-strips and about 0.1° in ϕ-direction by ϕ-strips. Fig. 21 summarizes the incident energy dependence of the position resolutions measured by the different longitudinal segment of the pad towers and by the θ- and ϕ-strips. Since the second longitudinal segment of the pads contains more than 80% of the shower energy , it gives the best resolution, whereas the first segment is poorer due to the larger fluctuation of the energy deposit even though the lateral profile is smaller. The strips, either of θ- or ϕ-strips, are almost a factor of two better because they are segmented four to five times smaller. The rapid improvement of the resolution for the first segment with increasing the energy is attributed to the improvement in the energy deposit fluctuation. For all the curves, only a gradual improvement is observed beyond 40 *GeV*. This is consistent with the trend of the shower profile which is essentially independent of the energy above 40 *GeV*.

8.8 ENERGY CALIBRATION RUN

In the final energy calibration runs, all 2304 pad towers were scanned by 100 *GeV* electron beams. The beam was injected into the center of every pad tower . An isometric plot of the anode wire response of one of the modules is shown in Fig.22 . Due to the lateral leakage the response is reduced at the peripheries of the quadrants. For the pads at the orthogonal edges the response was reduced to 50 to 95 % of the normal values in the central region. At the circular periphery of the outer circumference, the response was 20 to 40 % of that of the central region due to the fact that the shower penetrated through the cylindrical side wall. Fig.23 shows the cross sections of the above plot at four azimuthal angles, as typical examples.

Fig.24 is a histogram of the gain at all data points for one of the modules except for one row of the data points at the periphery of every quadrants. With the only correction applied to the data being the normalization for the gas gain using the monitoring tube data, the uniformity is 2.5 % or better for all of the quadrants. It improved to 2 % when two more rows of data points at the periphery of every quadrant were excluded as shown in Fig. 25 .

One of the aspects on the uniformity of the pad response is shown in Figs.26 *a* and *b* . The measured responses are averaged over the 16 pads in each of the 72 radial rows of $\Delta\phi = 5^\circ$ in Fig.26 *a* , and all 72 pads in a circular ring of pad rows of each of different η are averaged to show the general trend of pad response with varying η in Fig.26 *b* . The gradual drop of the response towards larger radius is due to the larger capacitances of the pad towers which reduces the gain of the charge-integrating amplifier by up to 20 % . Such effect will be eliminated once the aforementioned input buffer circuits are implemented for the second longitudinal segments.

8.9 GAIN CORRECTION

Once such a response map is measured, it is possible to correct the energy of the incident electrons for the local nonuniformity of the spot of the incidence on event-by-event basis. The gain correction factor a_i of the i- th pad tower, adding all three longitudinal segments, was calculated by minimizing χ^2 defined by the following formula,

$$\chi^2 = \sum_k \left(\sum_i a_i A_{ik} + \sum_j A_{jk} - M \right)^2 \qquad (4),$$

where M is the ideal gain constant over the entire surface, and A_{ik} is the signal of the i- th tower for the k-th event . The suffix j in the second term without the gain correction factor runs over the towers along the periphery of a quadrant, which have large leakage, and the suffix i runs over all other towers inside.

The validity of such correction was tested in the following procedure. In this test only the middle $\Delta\phi = 30^\circ$ sector of one of the quadrant modules was used. Therefore the peripheral 40 pad towers were used for the entry data for the second term without the correction factors and the 56 towers in the middle area between 10° and 30° in θ were used for the entry to the first term in the above formula. Fig.27 *a* is a raw distribution of the response from pad towers with scanning with 100 *GeV* electron beam along a radial line. Fig.27 *b* is a corresponding event-by-event distribution after the correction. Then the method was tested by using data samples for which the beam was injected along one of the radial boundaries between adjacent radial rows of towers and were not used as the input data to calculate the gain correction factors. The resulting distribution is shown in Fig.28 . The r.m.s. spread of 1.3 % is inclusive of several factors. If all the data in a 360° end plug is used as the entry the propagated error from the uncorrected entry data for the radial boundary will be largely eliminated even though there are decrease of the gain at those boundaries. The remaining factors are the intrinsic energy resolution and the local gain variation within each pad tower. Considering these the test is a proof of the validity of such method.

8.10 PION REJECTION

In most circumstances effective tool to identify electrons is to demand that the shower energy measured by the electromagnetic calorimeter is close to the momentum measured by a tracking device in front. However it is not quite usable in the angular region of the end plug calorimeter because the particles traverse the corner of the central tracking chamber resulting in inferior momentum resolution. Therefore it is desirable to develop a method to identify electrons without depending on the momentum measurement. A method based on a covariant matrix of longitudinal shower profile with correlation[14] was atudied[15]. The covariant matrix is defined as follows:

$$M_{ij}(E) = \frac{1}{N} \sum_{n=1}^{N} \left(X_i^{(n)}(E) - \langle X_i(E) \rangle \right) \left(X_j^{(n)}(E) - \langle X_j(E) \rangle \right) \qquad (5)$$

where N , $X_i^{(n)}$, and $\langle X_i \rangle$ stand for the total number of electron events, i-th variable of n-th electron event, and the mean value of the i-th variable, respectively. Then a variable ζ_k is defined for the k -th event to be tested as follows:

$$\zeta_k = \frac{1}{N_F} \sum_{i,j=1}^{L} \left(X_i^{(k)} - \langle X_i(E) \rangle \right) \left(M^{-1}(E) \right)_{ij} \left(X_j^{(k)} - \langle X_j(E) \rangle \right) \qquad (6),$$

where N_F denotes the number of the degrees of freedom and L is the total number of variables. M^{-1} is the inverse matrix of M defined by Eq.(5). $X_i^{(k)}$ and $\langle X_i \rangle$ are the i-th variable of the k-th event to be tested and the mean value of i-th variables for all tested events, respectively.

If the particle is completely isolated, layer-by-layer signals of all 34 anode wire planes in a quadrant can be used as the variables. However for the generality we use the pad- and strip-tower signals in order to avoid multiple event overlap. The following eight quantities were used; EM_1, EM_2', EM_3', H', θ', ϕ', σ_θ, and σ_ϕ . These are the energy deposits in the first, second and third pad tower segments in the elctromagnetic calorimeter, the energy deposit in the hadron calorimeter in the same projective tower, and the energy deposits in θ- and ϕ-strips, respectively, all normalized by the total energy deposit in the electromagnetic calorimeter. The last two quantities are the r.m.s lateral shower profile measured by the θ- and ϕ-strips. Fig. 29 is a plot of such fractional energy containments in the first and the second longitudinal segments against the incident energies. It is seen that they are almost constant beyond 70 GeV. Also only gradual dependence on the energy was observed in th matrix elements beyond 70 GeV . Therefore the matrix, whose elements are normalized by the total energy, to be used need not to be exactly of the observed energy. Figs.30 a , b , c , and d are the scatter plots of these quantities to show the correlation. The average values of the above quantities for 40 and 100 GeV are listed in Table 5.

Various combinations of the quantities were studied for sample events of 40 and 100 GeV electrons and pions. For example, fractional numbers of events are histogramed as a function of the parameter ζ in Fig.31 in which the first four quantities, $EM_{1,2,3}$ and H were used to calculate ζ. In Fig.32 the pion rejection was tested for various combinations of quantities which are marked on the curves. In this case 100 GeV pions were tested using a matrix for 100-GeV electrons. As seen from the figure, a rejection of a factor of 500 to 1000 can be achieved if an efficiency of 60 to 80 % for electrons is acceptable.

9. CONCLUSIONS

Two large lead-proportional tube sandwitch type calorimeters have been built and installed onto the central CDF detector structure to cover an angular region of 10° to 36° with respect to the baem line both in the forward and backward directions . A well defined projective tower geometry was formed by pad and strip read-out taking advantage of electrical transparency of conductive plastic material of the proportional tubes. After basic characteristics were explored, all 2304 pad towers were calibrated by 100 GeV electron beam. The gain uniformity of one of the modules was measured to be better than 2.5 % except for the peripheral area of quadrants. A χ^2-minimization procedure was explored to correct for the tower to tower gain variation using the measured response map. The uniformity was improved to 1.3 % in r.m.s. .
Capability of rejecting pions against electrons without relying on the momentum measurement was studied using a covariant matrix with longitudinal shower correlation. A rejection factor of 500 to 1000 was obtained for 100 GeV pions with 60 to 80 % efficiency for electrons. Table 6 summarizes the performance of the calorimeter.

ACKNOWLEDGEMENTS

The authors wish to express their sincere thanks to J. Robb and J. Rauch for their contribution throughout the design and construction of the calorimeter. Special thanks are due to J.Grimson and J. Omera for their advice on the design. T. Thomas, C. Olson, D. Beckner, J. Quattrochi, J. Wish, and R. Martin are thanked for their technical support. We owe great deal to M. Atac for important advices on many aspects of the project. We have been significantly benefitted from the work done by many other collaborators of CDF and are grateful to R. Schwitters, A. Tollestrup, and D. Theriot for discussions and support throughout the work. The authors are indebted to the Fermilab Research Division and the Fermilab Directorate for their kind arrangement for us as visitors at Fermilab. The work was supported by the Ministry of Education, Science, and Culture of Japan, and the U.S. Department of Energy under Contract DE-AC02-76-CH0-3000.

REFERENCES

(1)

	Lead with 0.065 % Ca + 0.7 % Sn	Lead with 6 % Sb
Ultimate Tensile Strength (*psi*)	9000	4400
Yield Strength (0.2 % Offset) (*psi*)	8500	2800
Elongation (%)	10	40
Stress Rupture (Hrs to Rupture @ Stress of 4000 *psi*)	50	Nil
(@ Stress of 3000 *psi*)	500	2

From Catalogue of St. Joe Lead Company, 7733 Forsyth Boulevard, Clayton, Missouri 63105.

(2) Y. Hayashide et al., Nucl. Instr. Meth. 204 (1983) 361.
Y. Hayashide et al., Nucl. Instr. Meth. 216 (1983) 127.

(3) Y. Fukui et al., Proc. Gas Sampling Calorimetry Workshop II, Fermilab , Oct.31-Nov.1, 1985, p1.
C. Bosio, et al., Nucl. Instr. Meth. 157 (1978) 35.

(4) Y. Fukui and Y. Hayashide, Fermilab CDF Note 267 (1984).

(5) M. Atac et al., Nucl. Instr. Meth. 200 (1982) 345.
M. Atac, IEEE Trans. Nucl. Sci. NS-31 (1984) 99.
M. Atac, Proc. Workshop on Radiation Damage to Wire Chambers, LBL, Jan.16-17, 1986.

(6) M. Atac et al., Fermilab CDF Note 477 (1986).

(7) S. Mikamo et al., Proc. Gas Calorimetr Workshop, Fermilab, Oct.28-29, 1982, p22.

(8) The pulse shape of the anode wire signal of the prototype module was consistent with the following basic understanding. The shower fills each of the involved tubes uniformly with secondary ionizations instantaneously. Then the electrons drift towards the anode wire with a constant velocity of about 5 *mm*/100 *nsec* . Since the signal we observe is not these elecrons but the avalanches induced by these electrons nearby the anode wire, ≤200 μm, the pulse shape is dependent on the drift distance r and the population within a ring of Δr which is proportional to $2\pi r \bullet \Delta r$ up to the peak corresponding to the largest ring at the distance of the wall. Then the differential area decreases towards the four corners of the tube cross section. Therefore for the 7 *mm* x 7 *mm* I.D. tube, the peak is at 70 *n sec* corresponding to the half of the gap, 3.5 *mm* , and the end of the signal is at 99 *n sec* corresponding to the distance to the corner , 4.95 *mm* . The actual signal is slowered from such basic structure by the effect of the ions drifting away from the anode wire which slowers the signal and make a long tail up to 100 μ *sec* .

(9) G. Drake et al., Being submitted to Nucl. Instr. Meth. in the same series as this paper.

(10) Isotopes Products Lab, 1800 N. Keystone Str., Burbank, CA 91504, Model No. CL-55.

(11) Y. Hayashide et al., IEEE Trans. Nucl. Sci. NS-30 (1983) 112.
Y. Hayashide et al., Nucl. Instr. Meth. 227 (1984) 452.
Y. Hayashide et al., Fermilab CDF Note 318 (1985).
(12) Y. Fukui, Fermilab CDF Note 266 (1984).
(13) Particle Data Group, Physics Letters 170B(1986)45.
(14) R. Engelmann et al., Nucl. Instr. Meth. 216 (1983) 45.
H. Miyata, Ph D Thesis, University of Tsukuba, 1984.
(15) Y. Fukui et al., Fermilab CDF Note 488 (1986).

Table 1 : MATERIAL THICKNESS

	Physical Thickness	Radiation Length	Pion Absorption Length
Front Cover Plate : Fe (z = 173.99 ~ 175.26 *cm*)	12.7 *mm*	0.722	0.05971
Each Sampling Layer (z = 175.26 ~ 226.06 *cm*)			
Lead Panel (Ca : 0.065 %, Sn : 0.7 %)	2.69 *mm*	0.480	0.0134
Chamber Layer			
Cu-Clad G-10	1.6 *mm*	0.013	0.0033
Conductive Plastic Tube (Wall: 0.8 *mm*, ID: 7.0 *mm* x 7.0 *mm*)	8.6 *mm*	0.007	0.0037
Cu-Clad G-10	1.6 *mm*	0.013	0.0033
Epoxy	0.2 *mm*		0.0003
50-μm G-10 (Only on Chambers wth Strips : 6-th ~ 15-th)	0.05 *mm*		0.0001
Total	12.1 *mm*	0.034	0.0107

TOTAL THICKNESS (FRONT COVER PLATE + 34 SAMPLING LAYERS)

$\theta = 0°$	51.4 *cm*	18.2 X_0	0.88 λ^{π}_{abs}
$\theta = 11°$ ($1/\cos\theta = 1.02$)		18.5 X_0	0.89 λ^{π}_{abs}
$\theta = 30°$ ($1/\cos\theta = 1.15$)		21.0 X_0	1.01 λ^{π}_{abs}

Table 2 : THE TYPES AND THE NUMBER OF THE SIGNALS

	η	$\Delta\eta$	No. of η-Segm.	$\Delta\phi$	No. of ϕ-Segm.	No. of Long. Segm.	No. of Modules	Total No. of Channels
PADS	1.13 ~ 1.2	0.07						
	1.2 ~ 1.32	0.06	16	5°	72	3	2	6912
	1.32 ~ 1.41	0.045						
	1.41 ~ 2.40	0.09						
θ-STRIPS	1.2 ~ 1.84	0.02	32	30°	12	1	2	768
ϕ-STRIPS	1.2 ~ 1.84	6.4	1	1°	30	1	2	720
ANODE WIRES : 156 wires in a $\Delta\phi$=90° chamber are ganged together. Layers No. 1 ~ 29 : R=132 *cm* ~ θ =11° Layers No.30 ~ 34 : R=125 *cm* ~ θ =11°			1	90°	4	34	2	272
MONITORING TUBES				Every ~30°		Two Places	2	48
TOTAL								8720 Channels

Table 3 : LONGITUDINAL LAYER CONFIGURATION

θ = 11°	30°	CHAMBER NO.	θ-STRIP	φ-STRIP	
1.24	1.41 X_0	1			PAD LONG. SEGMENT - I
		2			
		...			
3.33	3.78 X_0	5			
3.86	4.37 X_0	6	θ–STRIP No. 1		PAD LONG. SEGMENT - II
		7		φ–STRIP No. 1	
		8	θ–STRIP No. 2		
		9		φ–STRIP No. 2	
		10	θ–STRIP No. 3		
		11		φ–STRIP No. 3	
		12	θ–STRIP No. 4		
		13		φ–STRIP No. 4	
		14	θ–STRIP No. 5		
8.57	9.71 X_0	15		φ–STRIP No. 5	
		16			
		17			
		...			
15.89	18.01 X_0	29			
16.41	18.60 X_0	30			PAD LONG. SEGMENT -III
		31			
		...			
18.50	20.97 X_0	34			

Table 4 : MECHANICAL PARAMETERS

GAS VESSEL

Outer Diameter	280.7 *cm*
Inner Diameter	61.0 *cm* at z = 172.7 *cm* (Front End of Front Cover)
($\theta = 10°$)	81.5 *cm* at z = 231.1 *cm* (Rear End of Rear Plate)

Total Weight with Calorimeter Loaded 12.4 *metric tons*

Total Inner Volume 2.9 *m*3

Total Gas Volume 1.2 m^3

CHAMBER -ABSORBER STACK

Lead Absorber Panel	Ca 0.065 %, Sn 0.7 %
	2.69 *mm* Thick

Chamber Layer : Sandwitch of P.C. Board with Pad Pattern, Conductive Plastic Proportional Tube Array, and P.C. Board with Strip Pattern or Ground Plane.

Conductive Plastic Tube	Polystyrene with Fine Grain Carbon Powder
	60 ~ 100 $k\Omega$ / *square*
	I.D = 7 *mm* x 7 *mm* , Wall = 0.8 *mm* Thick
Anode Wire	50 μm Gold Plated Tungsten
	Tension ~150 *gr*
P.C. Boards	1.6 *mm* Thick, Copper Clad
Gas	Ar- Ethane 50 % - 50 %
	Isopropyl Alcohol ($-3\ °C$) 0.9%
H. V.	1.7 *kV* (Monitoring Tubes : 1.9 *kV*)

Table 5 : AVERAGE VALUES OF THE QUANTITIES USED IN EQ.(6) FOR ELECTRON IDENTIFICATION, FOR 40 *GeV* AND 100 *GeV* ELECTRONS

	40 *GeV* Electrons		100 *GeV* Electrons	
	Mean	r.m.s.	Mean	r.m.s.
EM_1'	0.082	0.032	0.050	0.020
EM_2'	0.893	0.036	0.909	0.024
EM_3'	0.025	0.023	0.041	0.018
H'	0.012	0.140	0.021	0.043
η'	0.236	0.036	0.207	0.034
ϕ'	0.212	0.025	0.191	0.026
σ_η (cm)	2.72	0.25	2.70	0.16
σ_ϕ (cm)	2.78	0.20	2.76	0.11

Note: $EM_{1,2,3}'$, H', η', and ϕ' are quantities normalized by the total energy deposited in the electromagnetic calorimeter, namely $EM_1 + EM_2 + EM_3$.

Table 6 : PERFORMANS OF THE CALORIMETER

Energy Resolution (Pad)			28 % / $\sqrt{E}$
Angular Resolution	: Second Pad Segment		$\Delta\theta$: 0.04° ~ 0.2°, $\Delta\phi$: 0.2° ~ 0.3°
	θ–Strips		$\Delta\theta$: 0.04°
	ϕ–Strips		$\Delta\phi$: 0.1°
Linearity at 200 GeV		1.8 kV	-16%
		1.7 kV	- 7 % (-4 % Leakage Inclusive)
Gain Uniformity (Anode Wire)			r.m.s. ≤ 2.5 %
Gain Monitoring			r.m.s. ≤ 0.5 %
Pion Rejection (Electron Efficiency 60 ~ 80 %)			500 ~ 1000 (100 GeV)

FIGURE CAPTIONS

Fig. 1 : Cross sectional view of the end plug electromagnetic calorimeter.

Fig. 2 : Exploded view of a layer of the proportional tube array, the p.c. board with pad patterns , and the p.c. board for ground plane.

Fig. 3 : Plastic anode wire support.

Fig. 4 : Patterns of the outside pick-up electrodes:

a : Pads.

b : θ-strips.

c : ϕ-strips.

Fig. 5 : Isometric view of a quadrant showing the projective pad tower structure and the longitudinal layers.

Fig. 6 : Isometric view of the gas vessel.

Fig. 7 : Gas flow diagram.

Fig. 8 : Typical Fe^{55} spectrum measured by one of the gain monitoring tubes at 1.9 kV.

Fig. 9 : Plots of 5.9 keV peaks of Fe^{55} sources mounted on 21 monitoring tubes distributed in one of the end plug calorimeter modules. Each of the peak values was normalized by the mean of all tubes. The data are for about two month period out of the five-month long CDF engineering run .

Fig.10 : Lego plot of the energy deposit of electrons measured by the projective pad towers.

Fig.11 : Longitudinal profile of the electron induced shower measured by the anode wire planes.

Fig.12 : Fractional r.m.s. fluctuation of the layer by layer energy deposit.

Fig.13 : Longitudinal shower leakage from the back of the calorimeter at 1.8 kV. Data points from 20 GeV up to 200 GeV were fitted by a curve of a form of $y = a E^b$ and extrapolated to higher enrgies. The leakage was calculated by extrapolating curves fitted to the tail of the shower beyond 15 radiation length to infinite thickness. The functional form of Eq. (3) was used. The other curves are the estimated longitudinal shower leakage at various incident angles using a parametrization derived from the above procedure.

Fig.14 : The resolution of the energy measured by the pads at 1.8 kV.

Fig.15 : Dependence of the energy resolution on the operating voltages.

Fig.16 : Scatter plot of the layer by layer response of the calorimeter:

a : 1.7 kV vs. 1.65 kV.

b : 1.85 kV vs. 1.65 kV.

Fig.17 : Response of each layer normalized to the response at 1.65kV. The ratios are further normalized for their absolute values using the ratios at the last eight layers.

Fig.18 : Energy dependence of the calorimeter response at 1.8 kV. The data was fitted by a

quadratic curve. The dotted line represents the linear term. The energy dependence at 1.7 kV using a parametrization is also shown.

Fig.19 : Scatter plots of the measured shower centroid against the angle of the tower measured by a rotary encoder. The rotary encoder readings were corrected for the event-by-event beam angle measured by the proportional chambers.

a : Measured by the second longitudinal segments of the pad towers.

b : Measured by the θ-strip towers.

Fig.20 : R.m.s. error in the position measurement by the second longitudinal segments of the pad towers:

a : θ-direction.

b : ϕ-direction.

Fig.21 : Incident energy dependence of the position resolution.

a : θ-direction.

b : ϕ-direction.

Fig.22 : Isometric plot of the anode wire response.

Fig.23 : Event by event plots of the summed anode wire signals at four azimuthal angles as the examples.

Fig.24 : Histogram of the anode wire signals for all the scanned points in one of the end plugs. Each entry is a mean value of the signals for 100 GeV electrons injected at the same spot. The data corresponding to one row of the pads around the periphery of every quadrant are excluded. Only correction applied to the data is for the gas gain using the monitoring tube data taken concurrently with the data.

Fig.25 : Histogram of all data in Fig. 24 except for three rows of data points at the periphery of every quadrant .

Fig.26 : Averaged pad responses of one of the end plugs.

a : Averaged over 16 pads in a radial row. The horizontal axis is the order of the radial rows of pads in ϕ, 72 altogether of $\Delta\phi = 5^{\circ}$ each.

b : Averaged over 72 pads in a circular rows of pads. The horizontal axis is the order of the circular rows of pads in radius, 16 altogether from inner to outer radii.

Fig.27 : Response of pads along radial lines at four different ϕ.

a : Raw data without gain correction.

b : The same data as the above after the gain correction.

Fig.28 : Plot of an independent data set ,which was not used as the input data for calculating the error matrix inversion of Eq.4, corrected by the gain correction factors.

Fig.29 : Fractional energy deposits in the first (R_0) amd the second (R_1) longitudinal segments of pad tower as a function of the incident energy.

Fig.30 : Scatter plots of the fractional energy deposits in the first (R_0) and the second (R_1) segments at four different energies, 20, 40, 100, and 200 GeV.

Fig.31 : Fractional number of sample events for the pion rejection test as a function of parameter ζ defied by Eq. (6). For definition of ζ see text.

Fig.32 : Pion rejection factor for various combinations of eight measured quantities. See text.

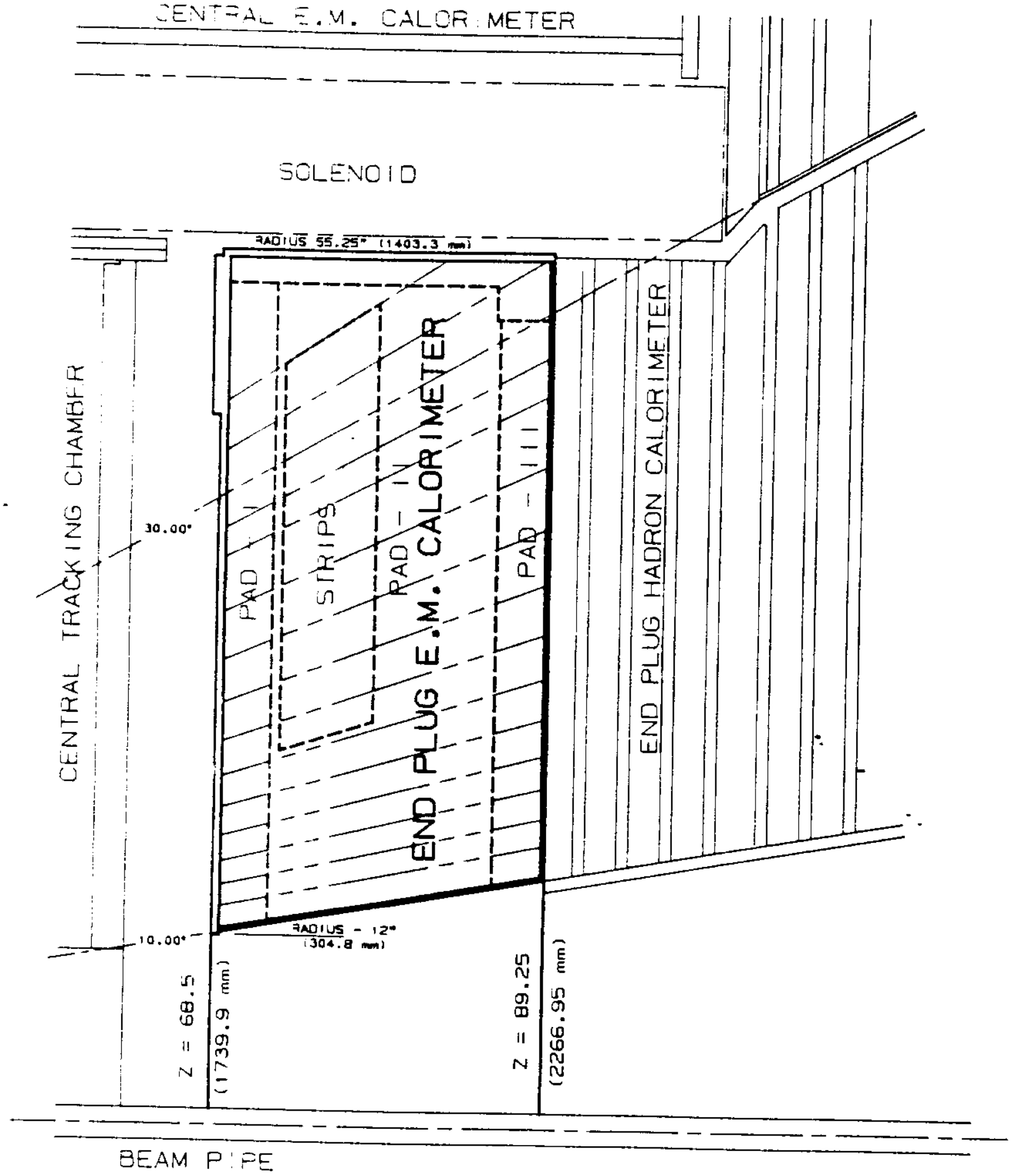
CENTRAL E.M. CALORIMETER
SOLENOID
RADIUS 55.25" (1403.3 mm)
CENTRAL TRACKING CHAMBER
30.00°
PAD - I
STRIPS
PAD - II
END PLUG E.M. CALORIMETER
PAD - III
END PLUG HADRON CALORIMETER
RADIUS - 12"
(304.8 mm)
10.00°
Z = 68.5
(1739.9 mm)
Z = 89.25
(2266.95 mm)
BEAM PIPE

Fig 1

3159

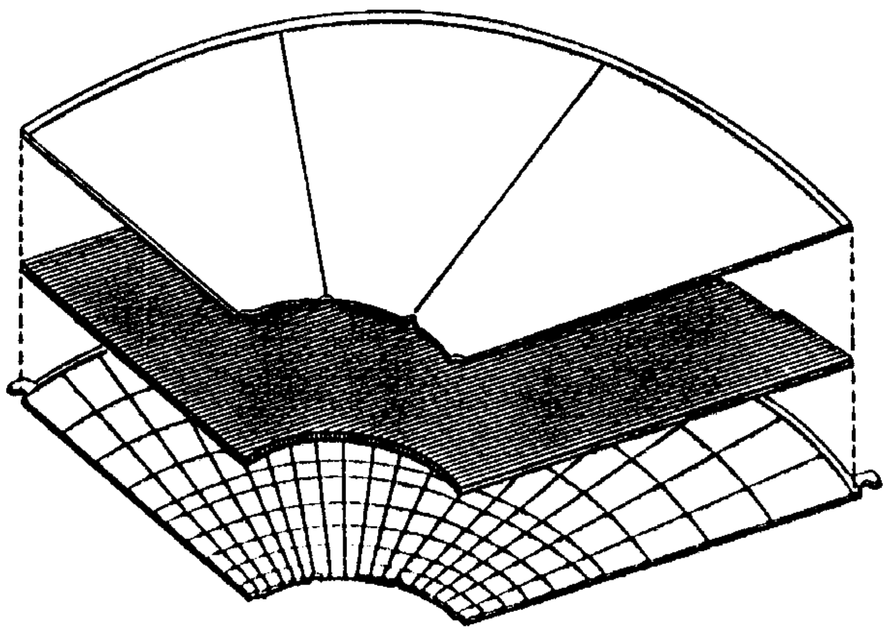

Fig. 2

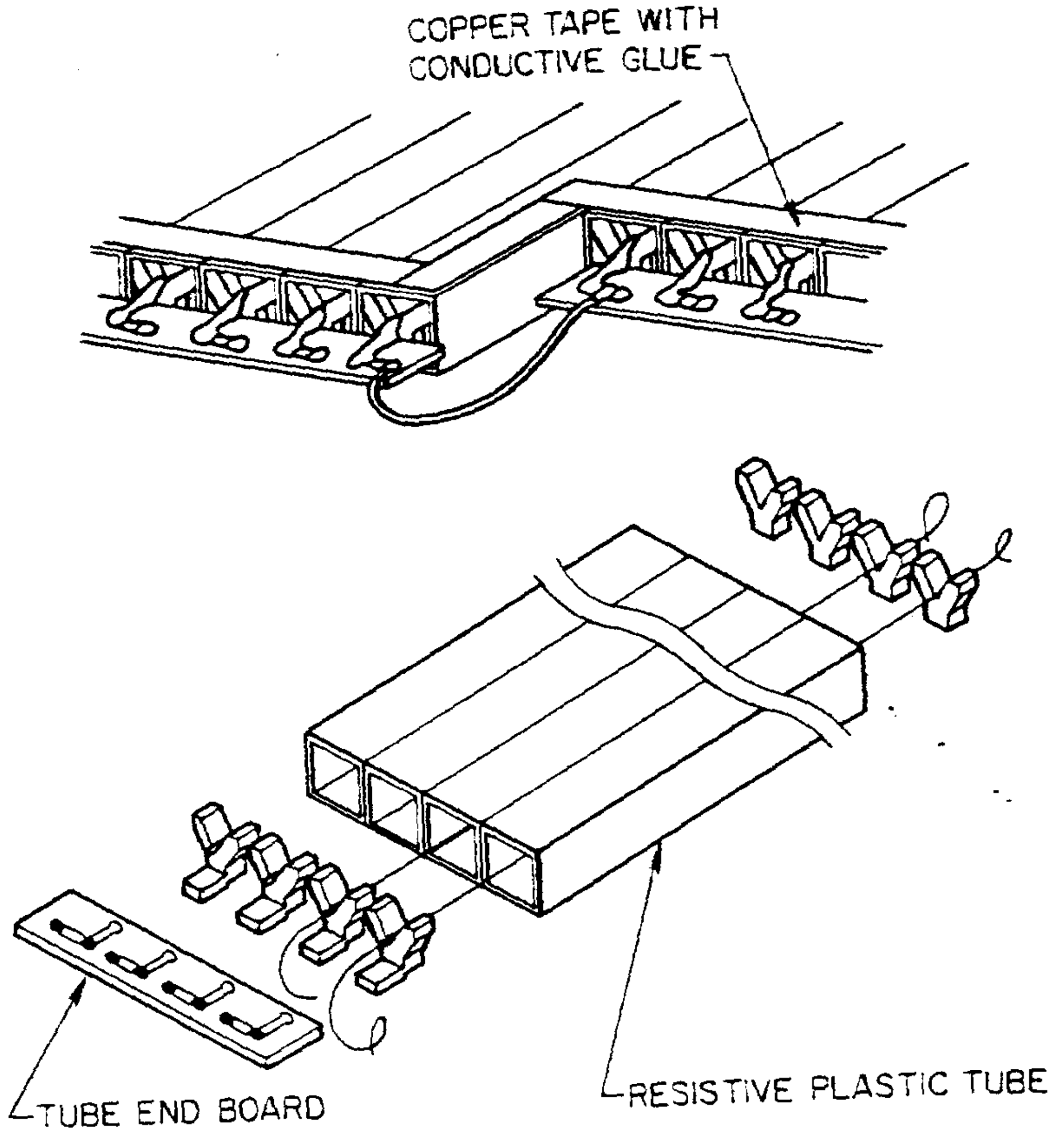
COPPER TAPE WITH
CONDUCTIVE GLUE
TUBE END BOARD
RESISTIVE PLASTIC TUBE

Fig. 3

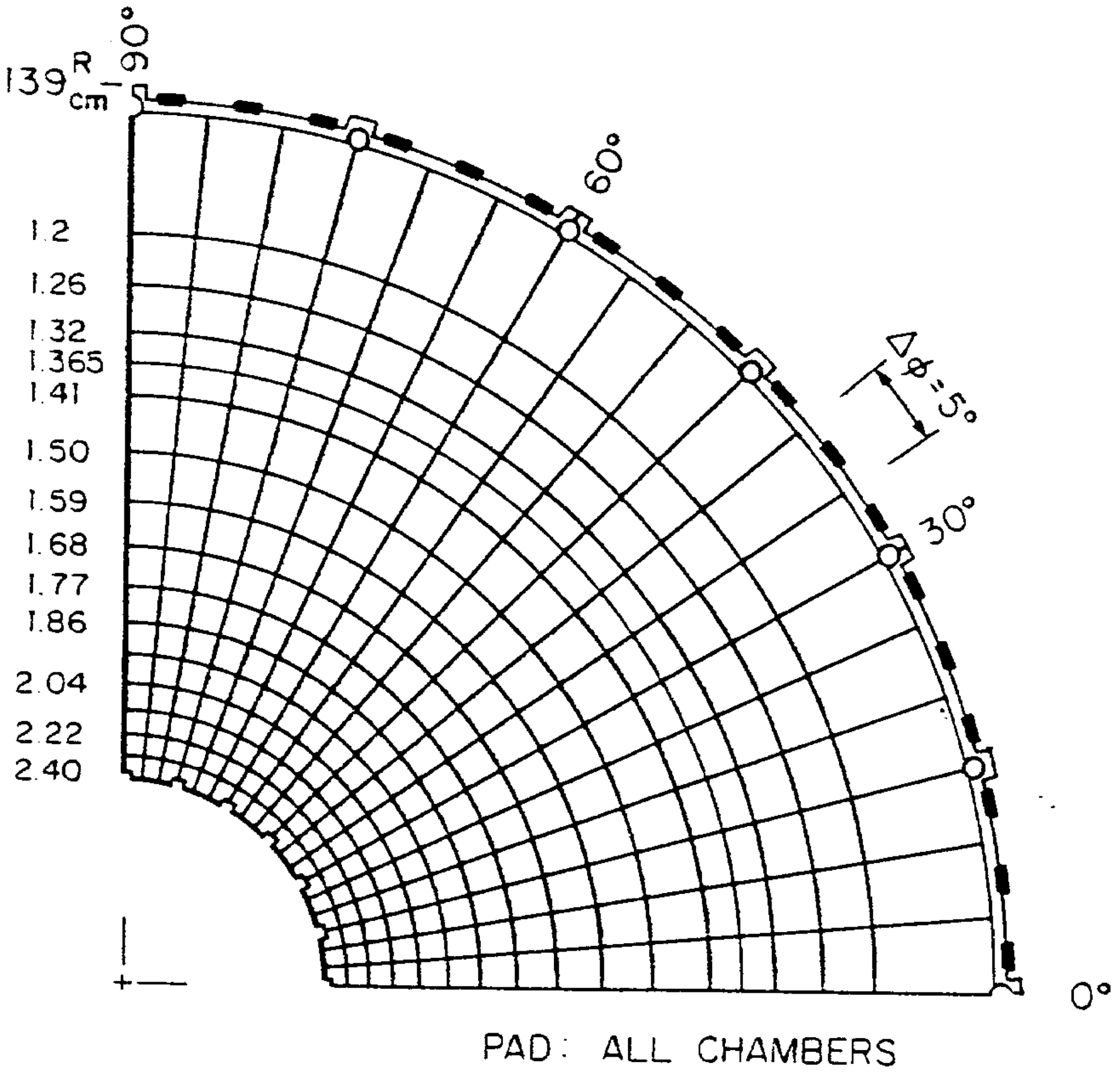

PAD: ALL CHAMBERS

Fig 4a

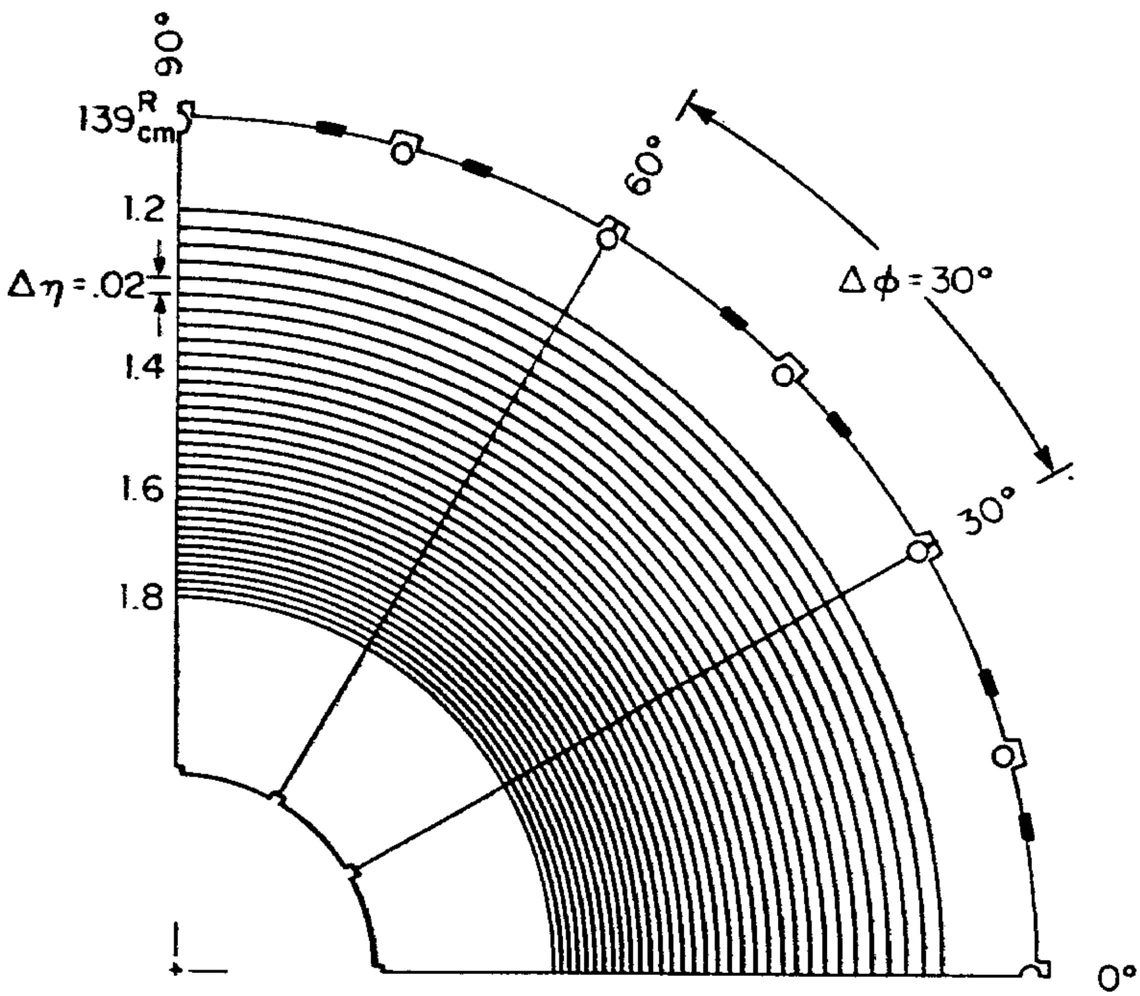

θ-STRIPS: CHAMBERS N.. 6,8,10,12,14

Fig. 47

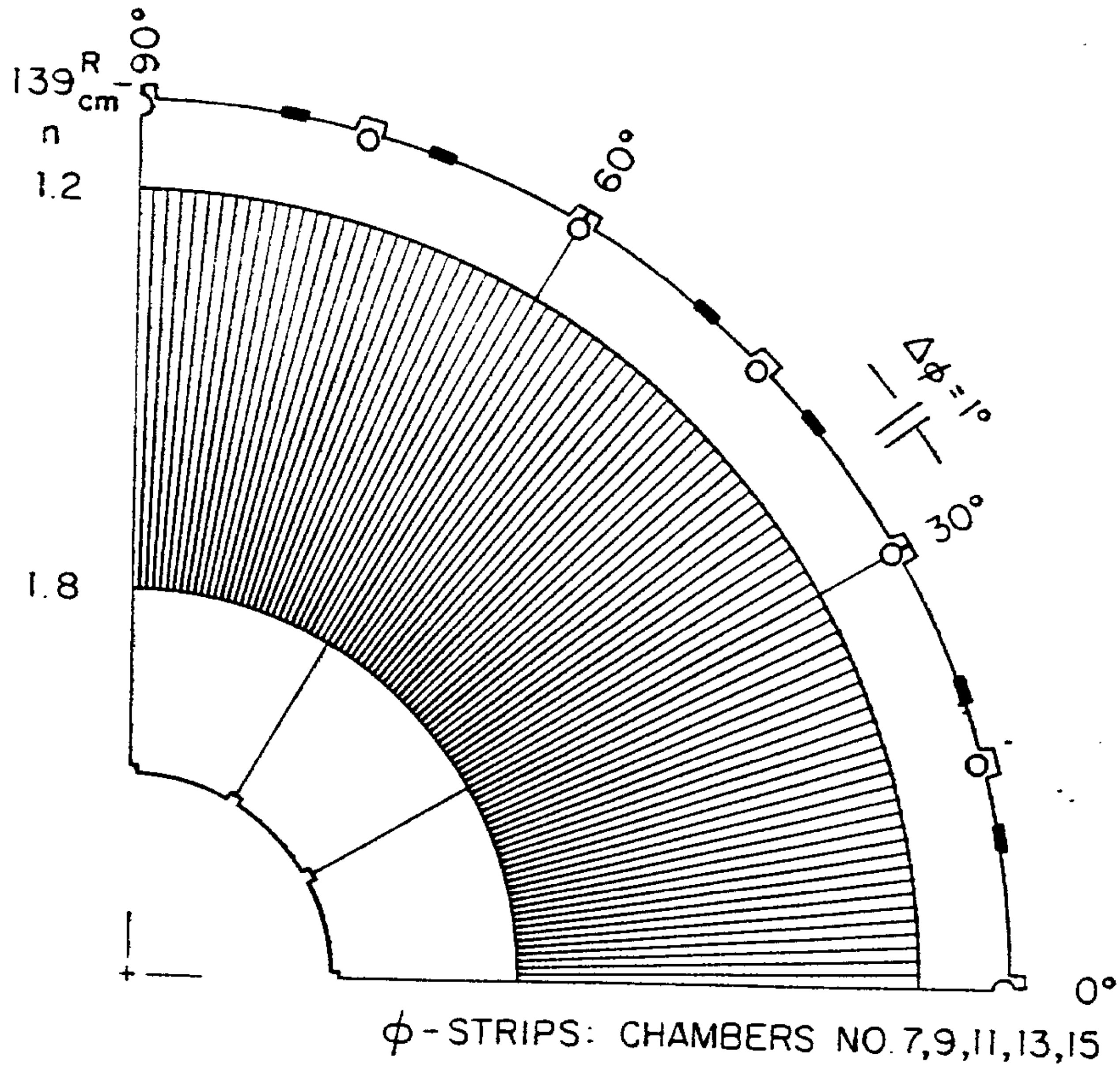

Fig 4c

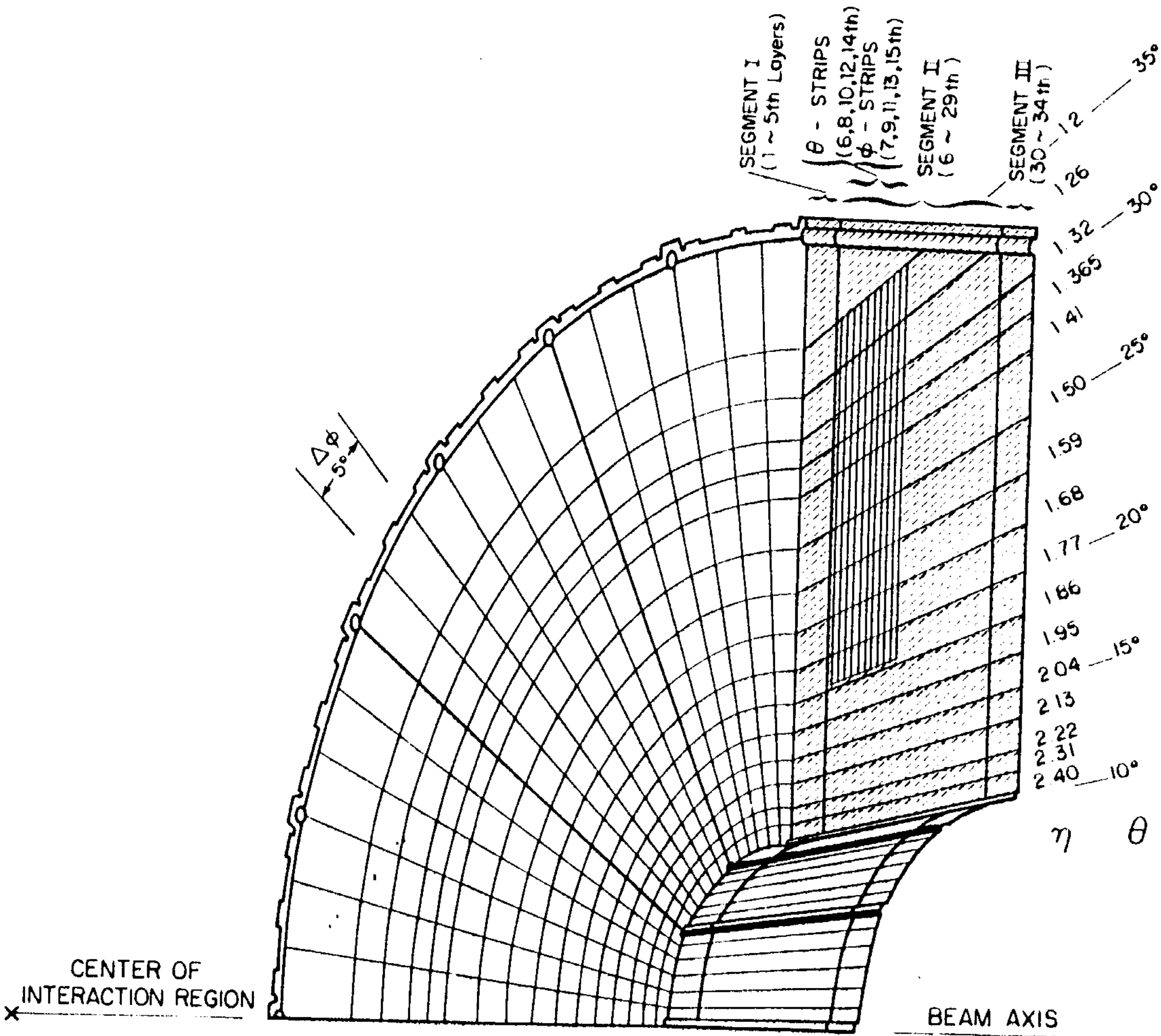

SEGMENT I
(1 ~ 5th Layers)
θ - STRIPS
(6,8,10,12,14th)
φ - STRIPS
(7,9,11,13,15th)
SEGMENT II
(6 ~ 29th)
SEGMENT III
(30 ~ 34th)
Δφ
5°
1.2
1.26
1.32
1.365
1.41
1.50
1.59
1.68
1.77
1.86
1.95
2.04
2.13
2.22
2.31
2.40
35°
30°
25°
20°
15°
10°
η
θ
CENTER OF INTERACTION REGION
BEAM AXIS

Fig 5

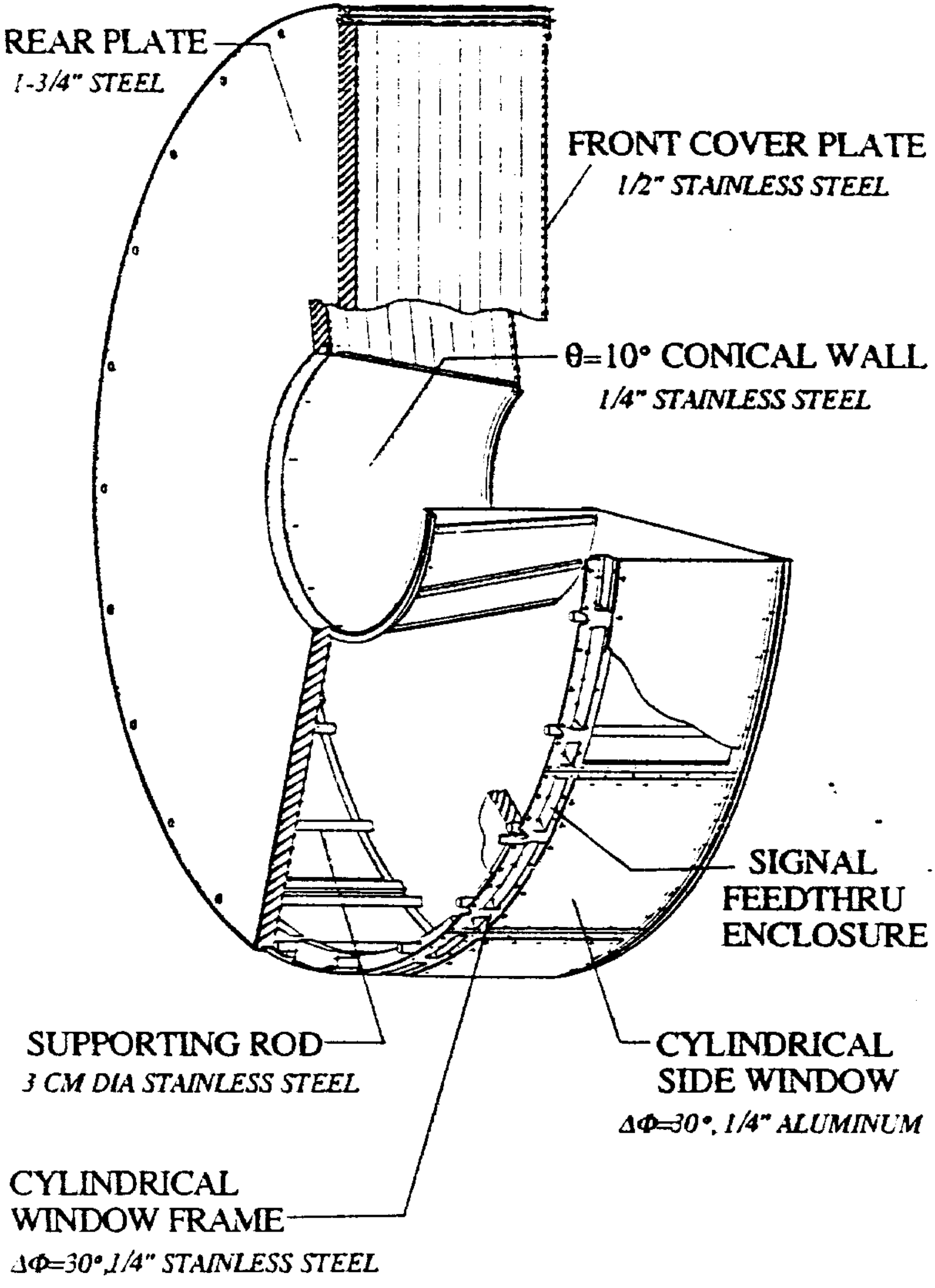

GAS VESSEL

Fig 6

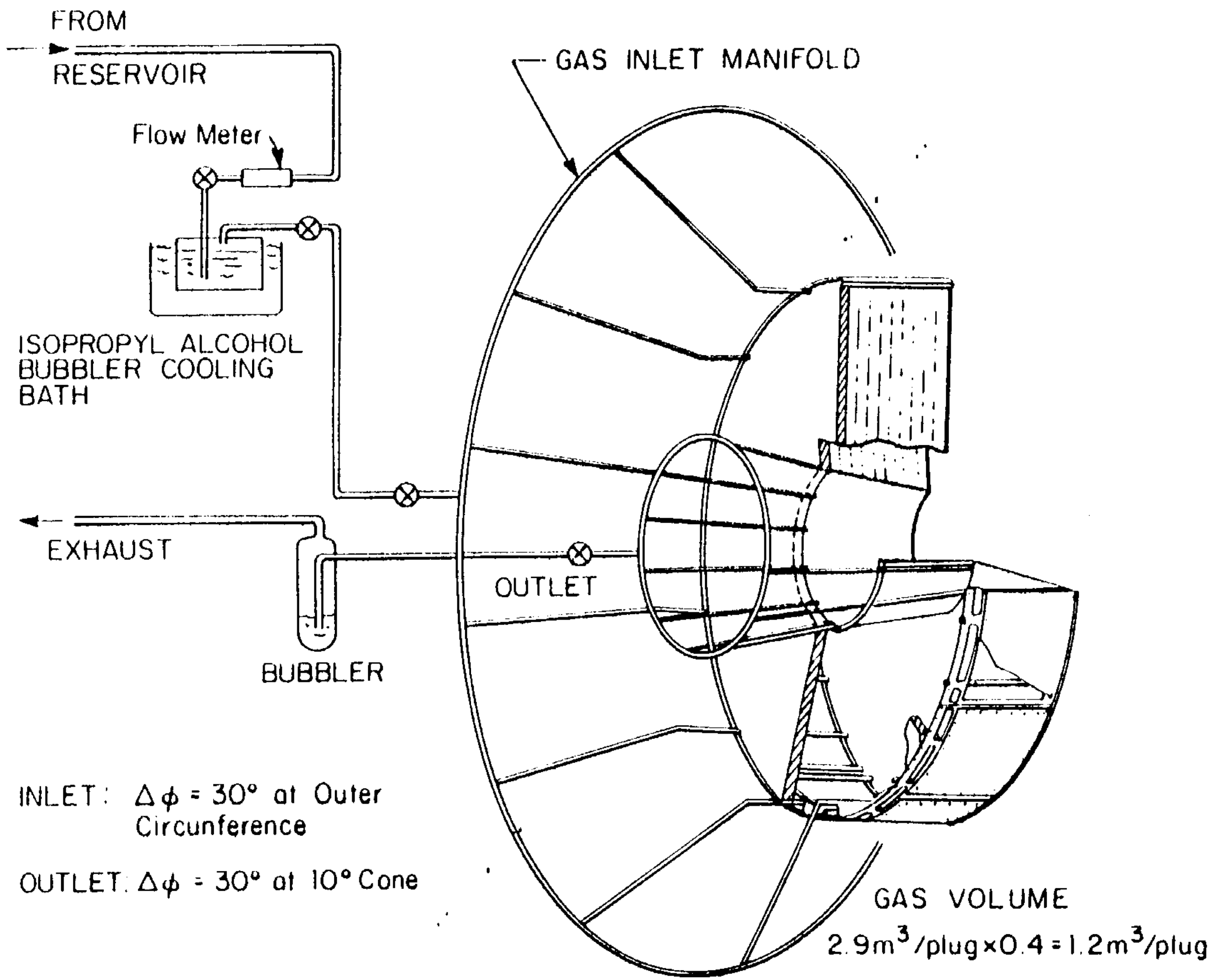
FROM
RESERVOIR
Flow Meter
ISOPROPYL ALCOHOL
BUBBLER COOLING
BATH
EXHAUST
BUBBLER
GAS INLET MANIFOLD
OUTLET
INLET: Δφ = 30° at Outer Circunference
OUTLET: Δφ = 30° at 10° Cone
GAS VOLUME
2.9m³/plug×0.4 = 1.2m³/plug

Fig. 7

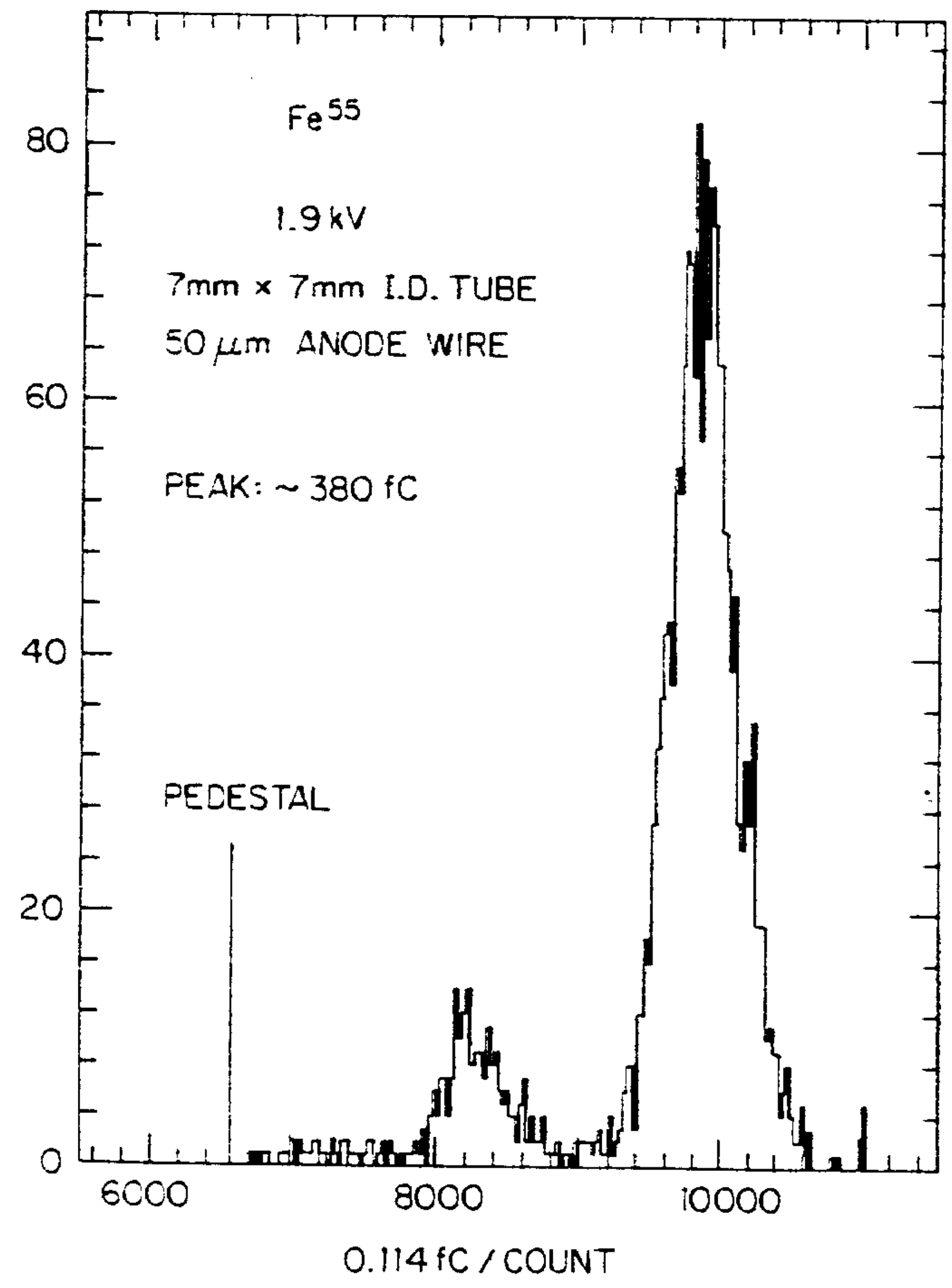
Fe55
1.9 kV
7mm × 7mm I.D. TUBE
50 μm ANODE WIRE
PEAK: ~ 380 fC
PEDESTAL
80
60
40
20
0
6000
8000
10000
0.114 fC / COUNT

Fig 8

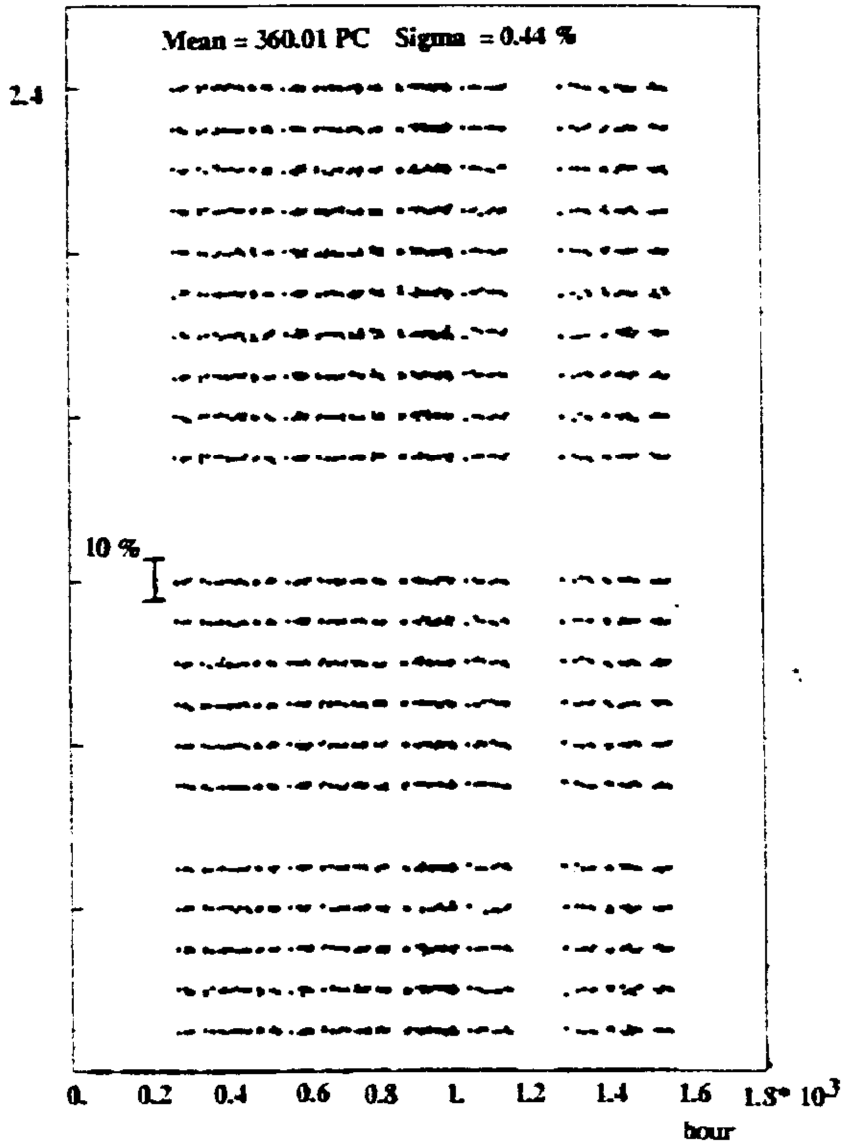

Fig 9

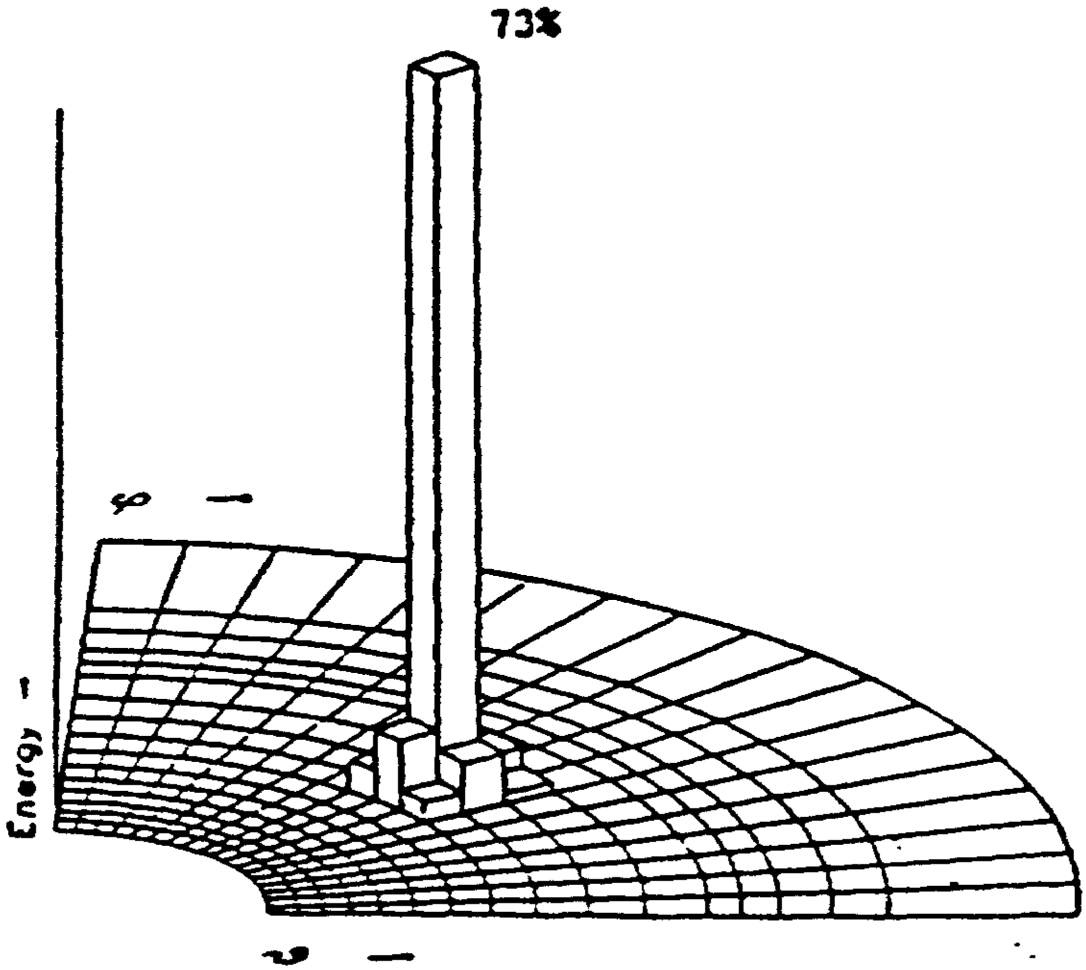

Fig. 10

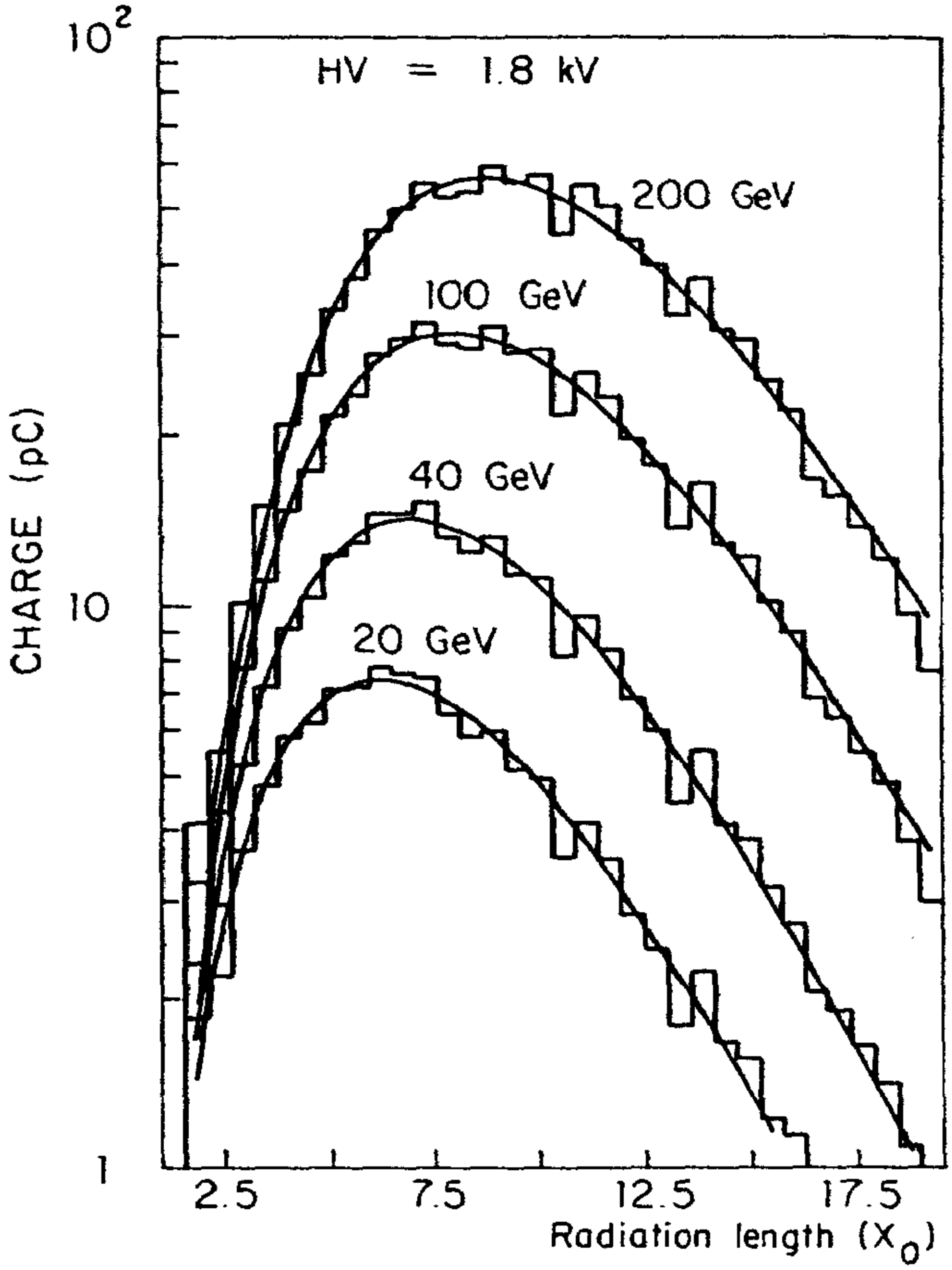

LONGITUDINAL SHOWER PROFILE

Fig. 11

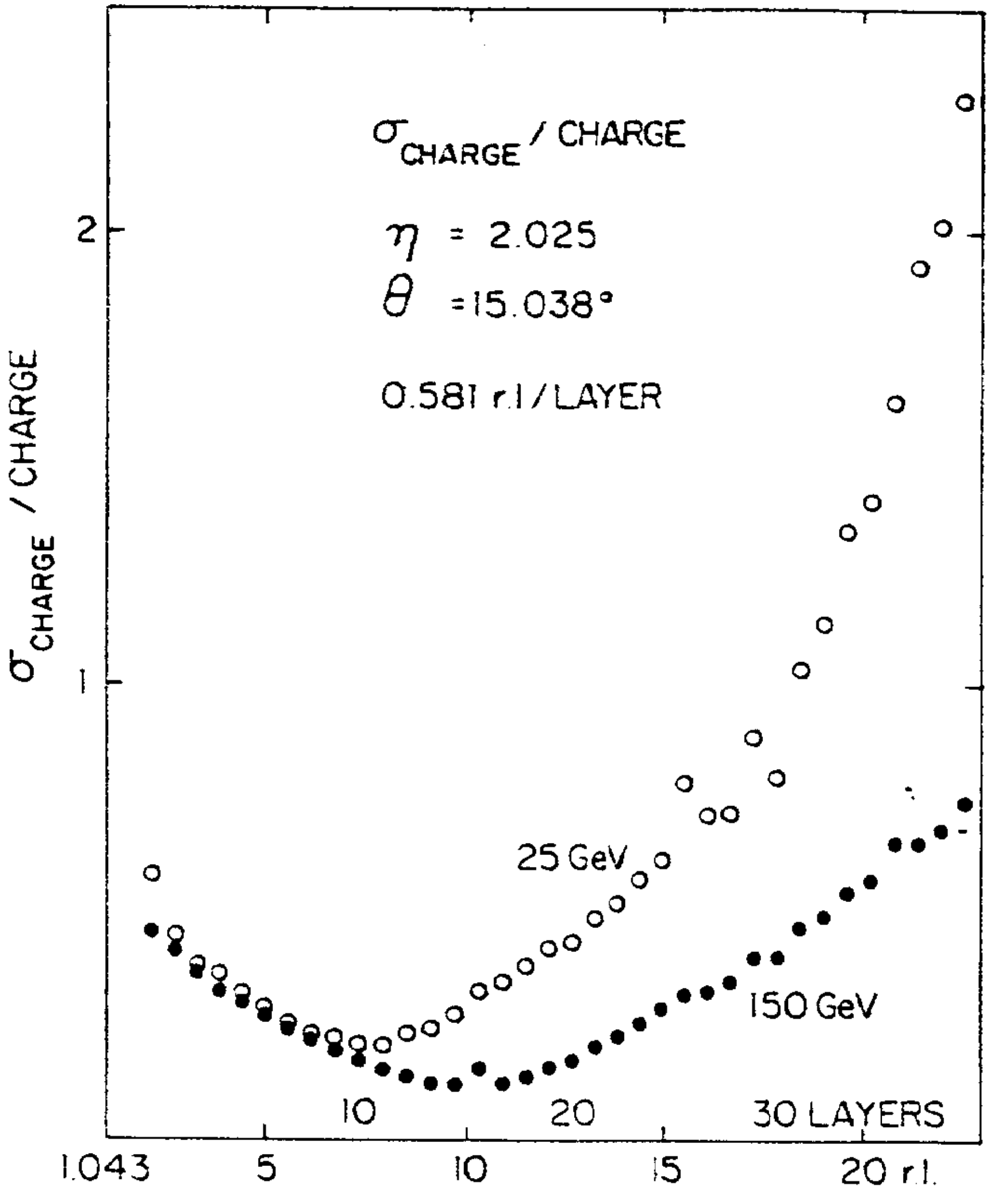
σ CHARGE / CHARGE
η = 2.025
θ = 15.038°
0.581 r.l / LAYER
25 GeV
150 GeV
10
20
30 LAYERS
1.043
5
10
15
20 r.l.
1
2

Fig. 12

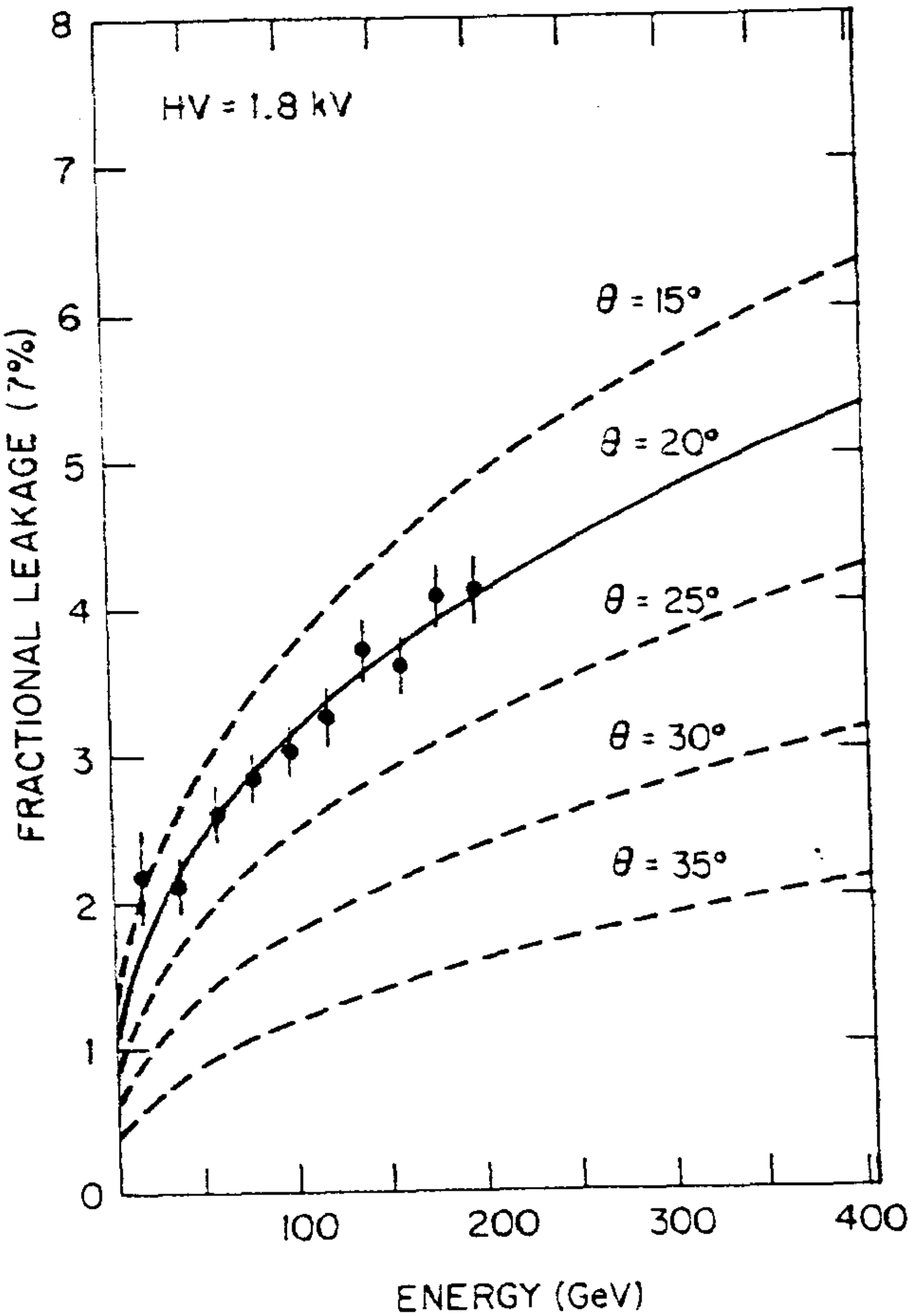

HV = 1.8 kV
θ = 15°
θ = 20°
θ = 25°
θ = 30°
θ = 35°
FRACTIONAL LEAKAGE (7%)
ENERGY (GeV)
0
1
2
3
4
5
6
7
8
100
200
300
400

Fig 13

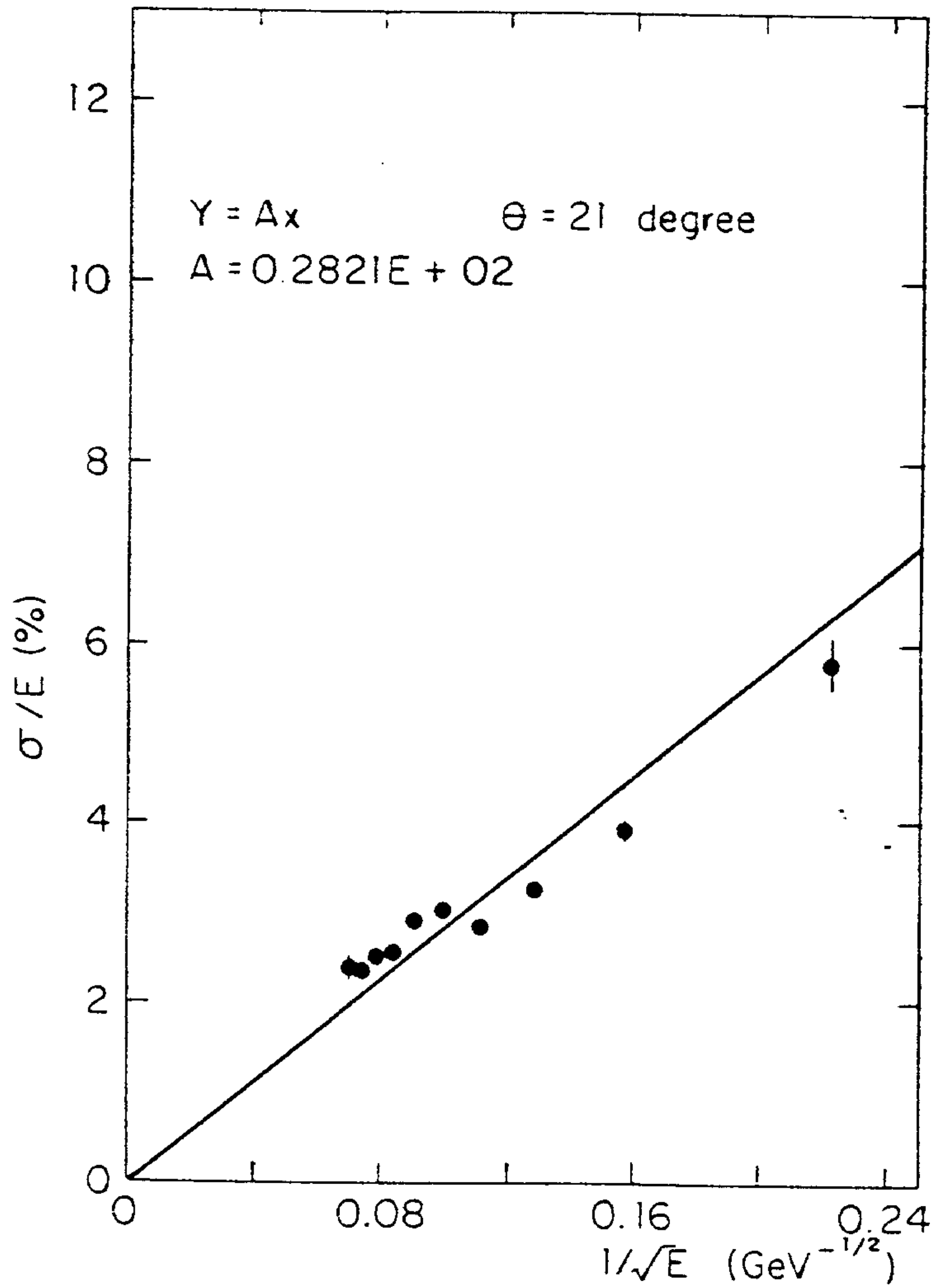

ENERGY RESOLUTION (PAD)

Fig. 14

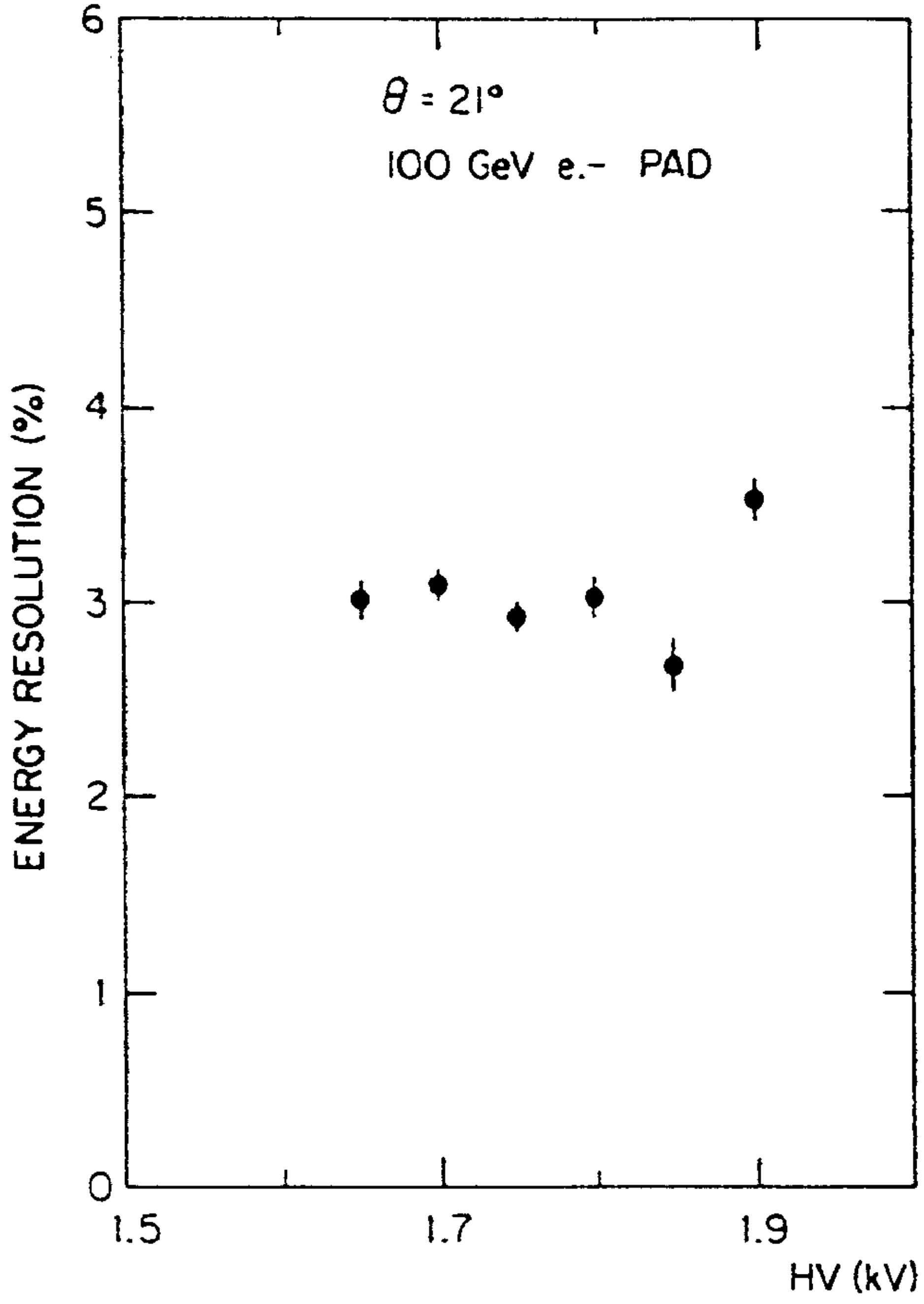

HV VS ENERGY RESOLUTION

Fig. 15

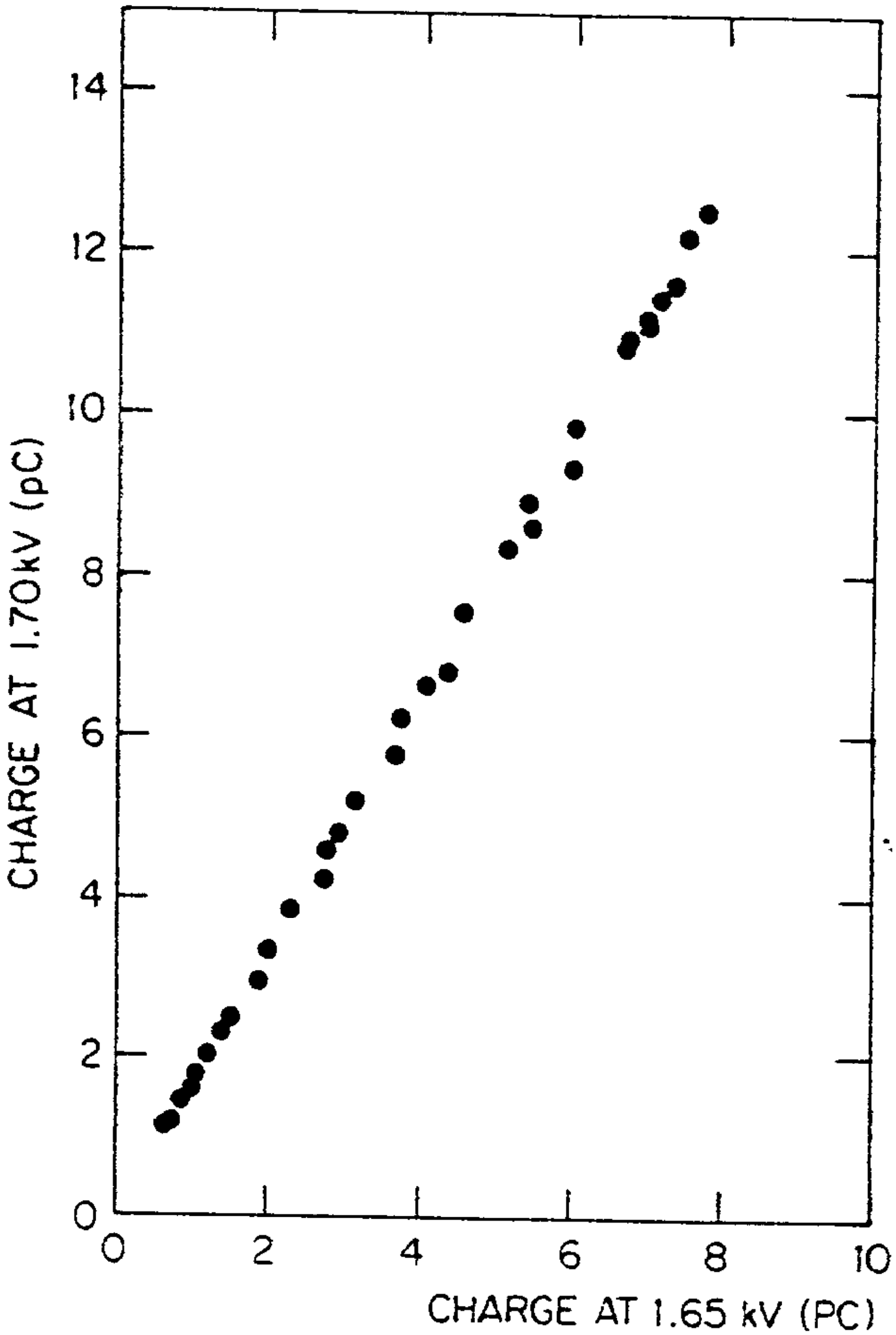

CHARGE AT EACH LAYER

Fig. 16 a

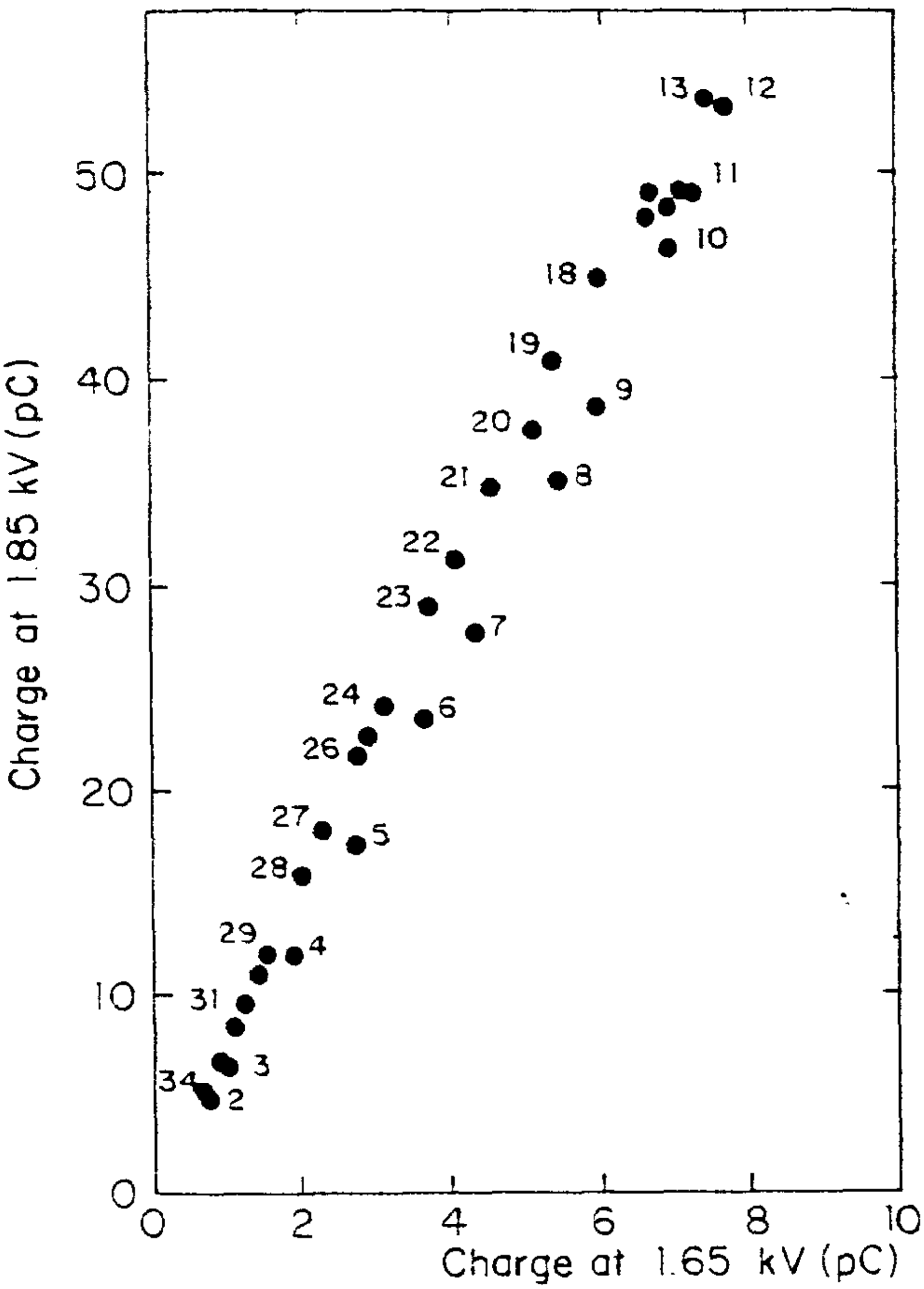

CHARGE AT EACH LAYER

Fig 16 b

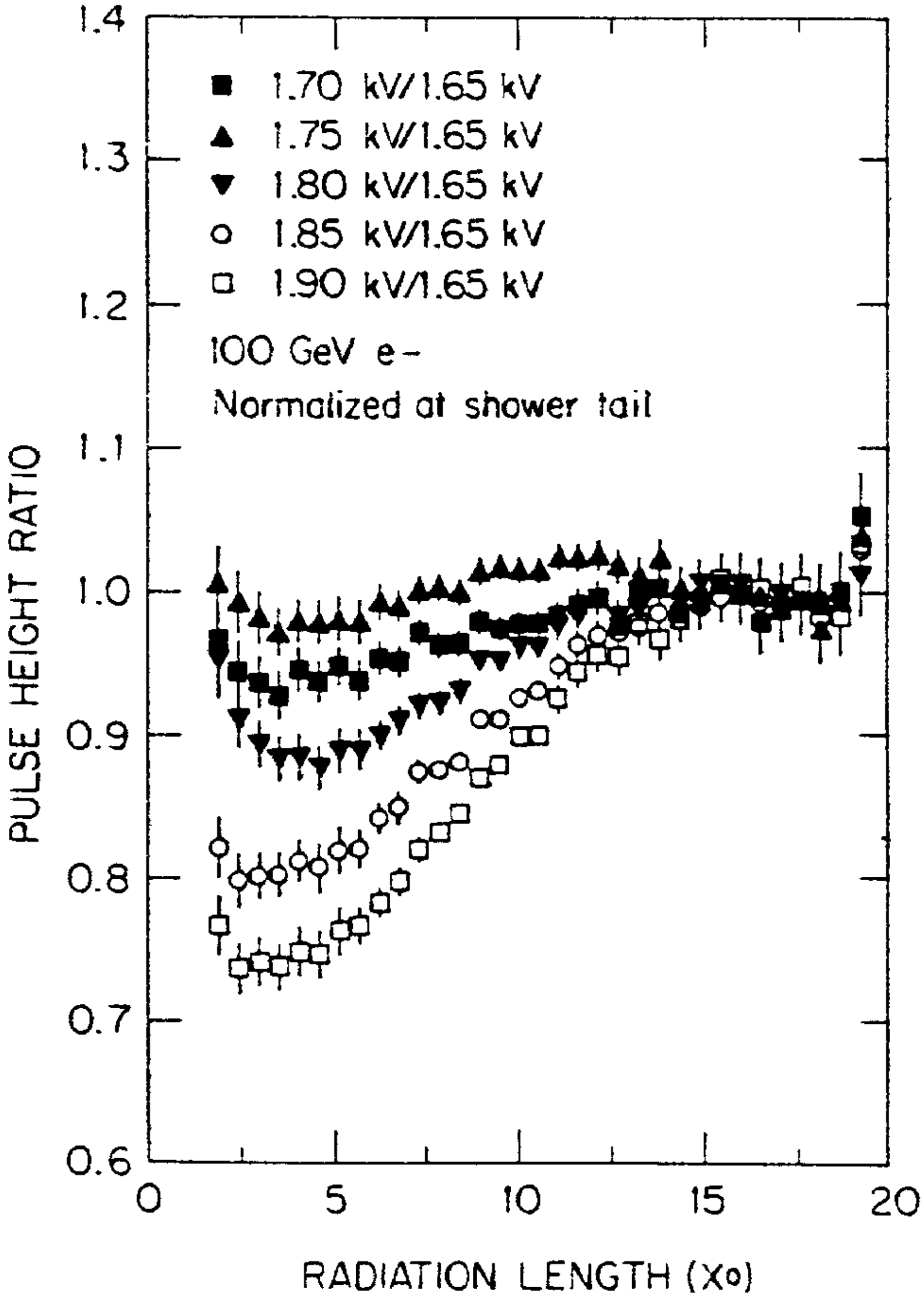

1.70 kV/1.65 kV
1.75 kV/1.65 kV
1.80 kV/1.65 kV
1.85 kV/1.65 kV
1.90 kV/1.65 kV
100 GeV e-
Normalized at shower tail
PULSE HEIGHT RATIO
RADIATION LENGTH (Xo)
1.4
1.3
1.2
1.1
1.0
0.9
0.8
0.7
0.6
0
5
10
15
20

Fig. 17

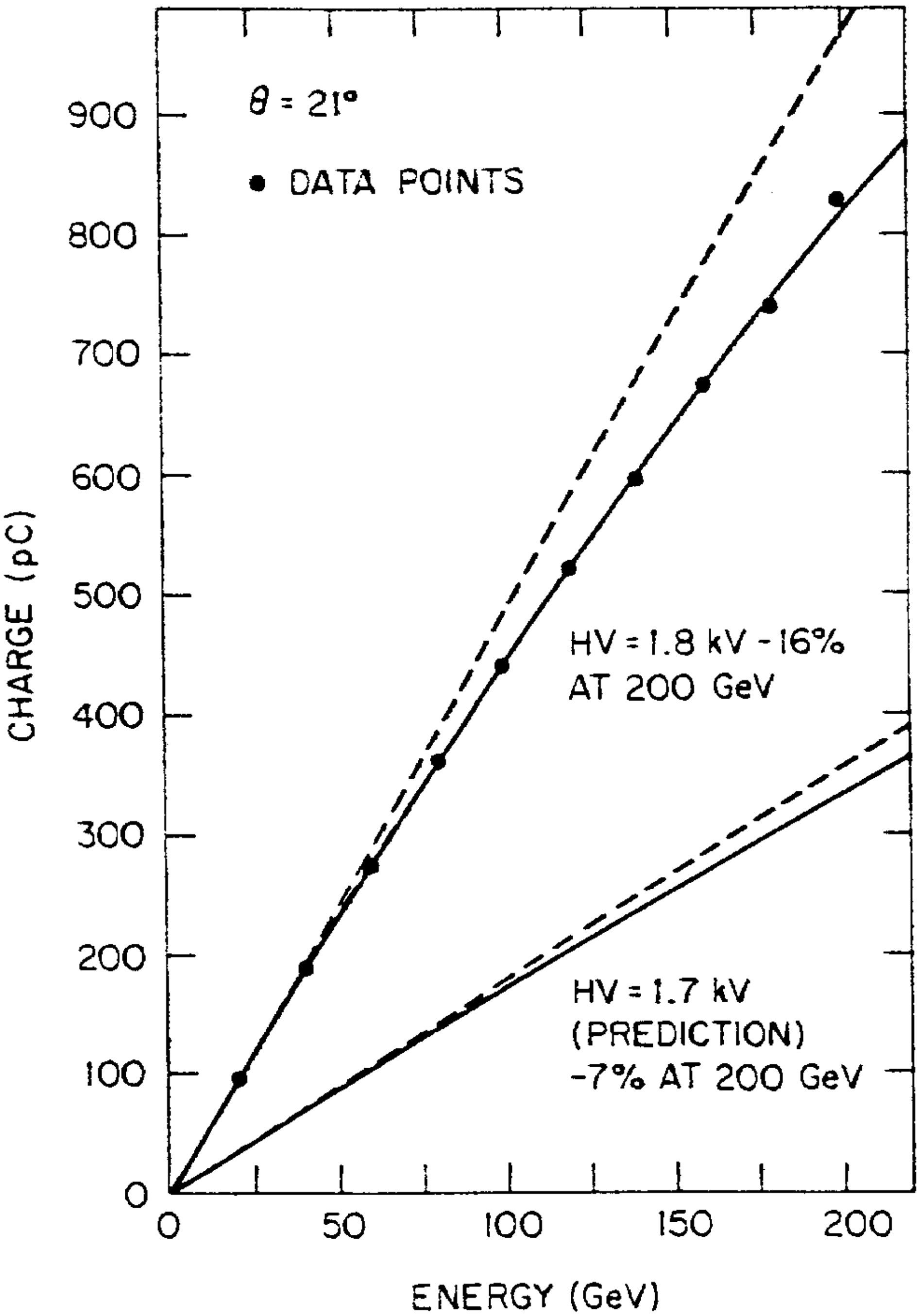
θ = 21°
● DATA POINTS
HV = 1.8 kV -16%
AT 200 GeV
HV = 1.7 kV
(PREDICTION)
-7% AT 200 GeV
CHARGE (pC)
ENERGY (GeV)
0
100
200
300
400
500
600
700
800
900
0
50
100
150
200

Fig. 18

a) by pad

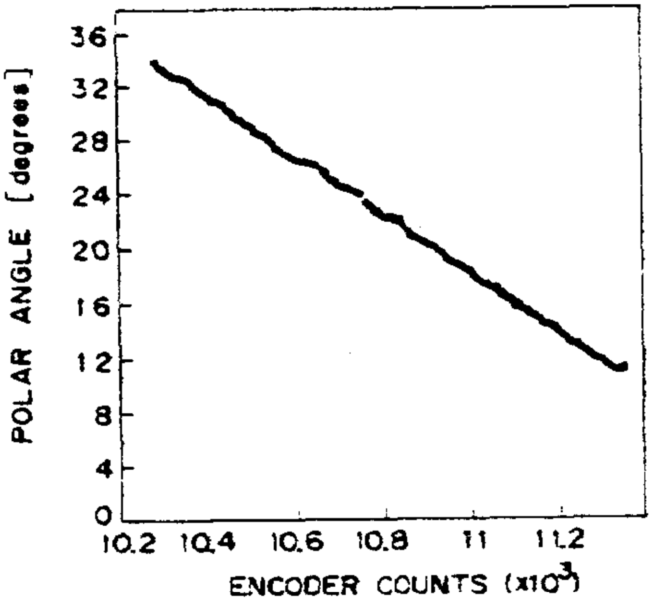

Fig. 19a

b) θ-strip

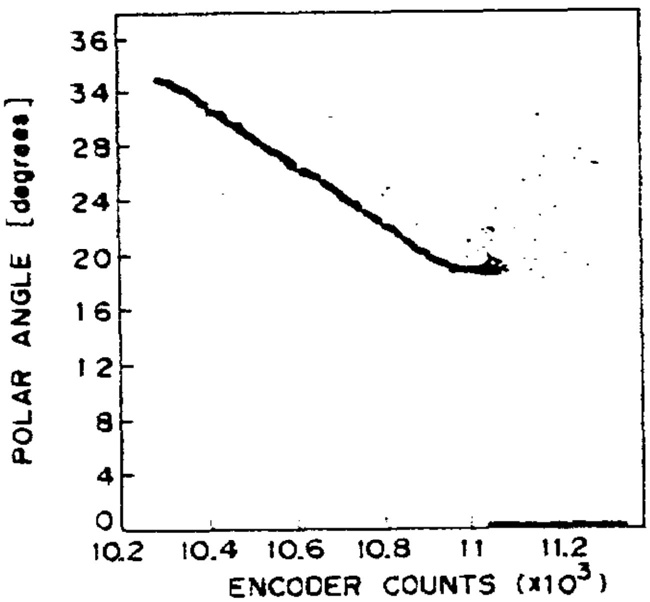

Fig 19b

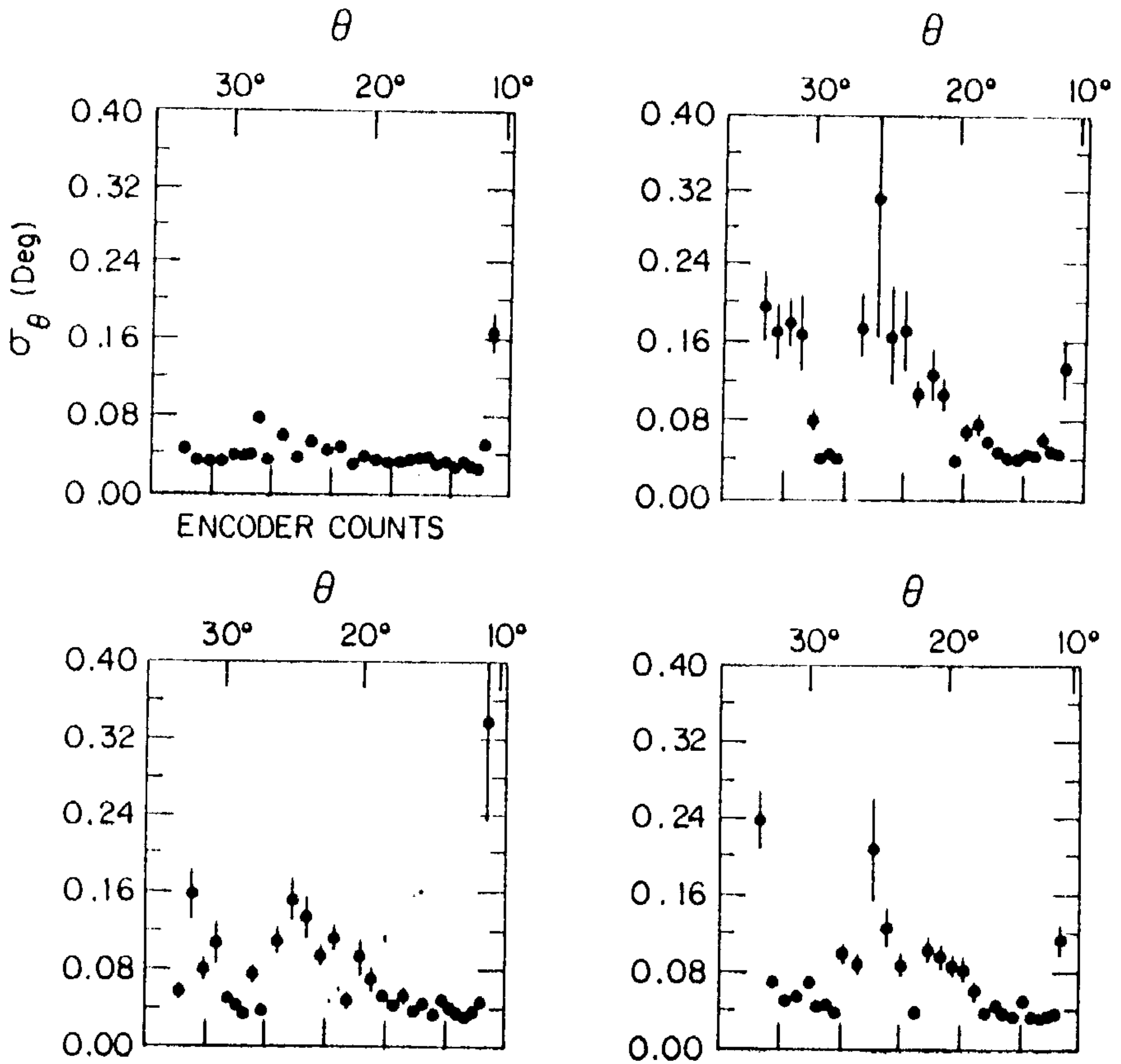

θ Resolution by Pad. Fig 20 a

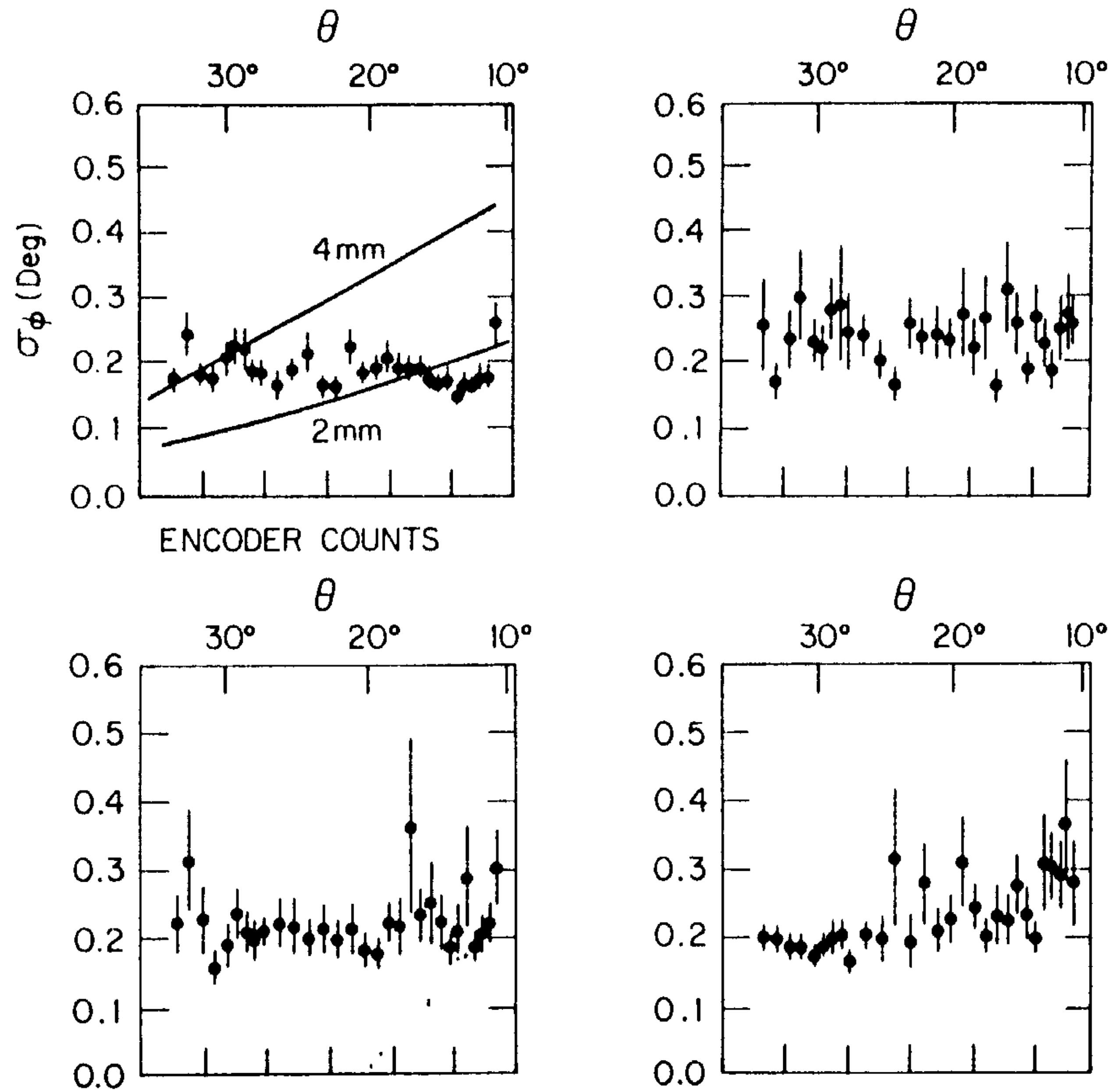

ϕ Resolution by Pad

Fig. 20 b

Electron Energy vs. Position Resolution

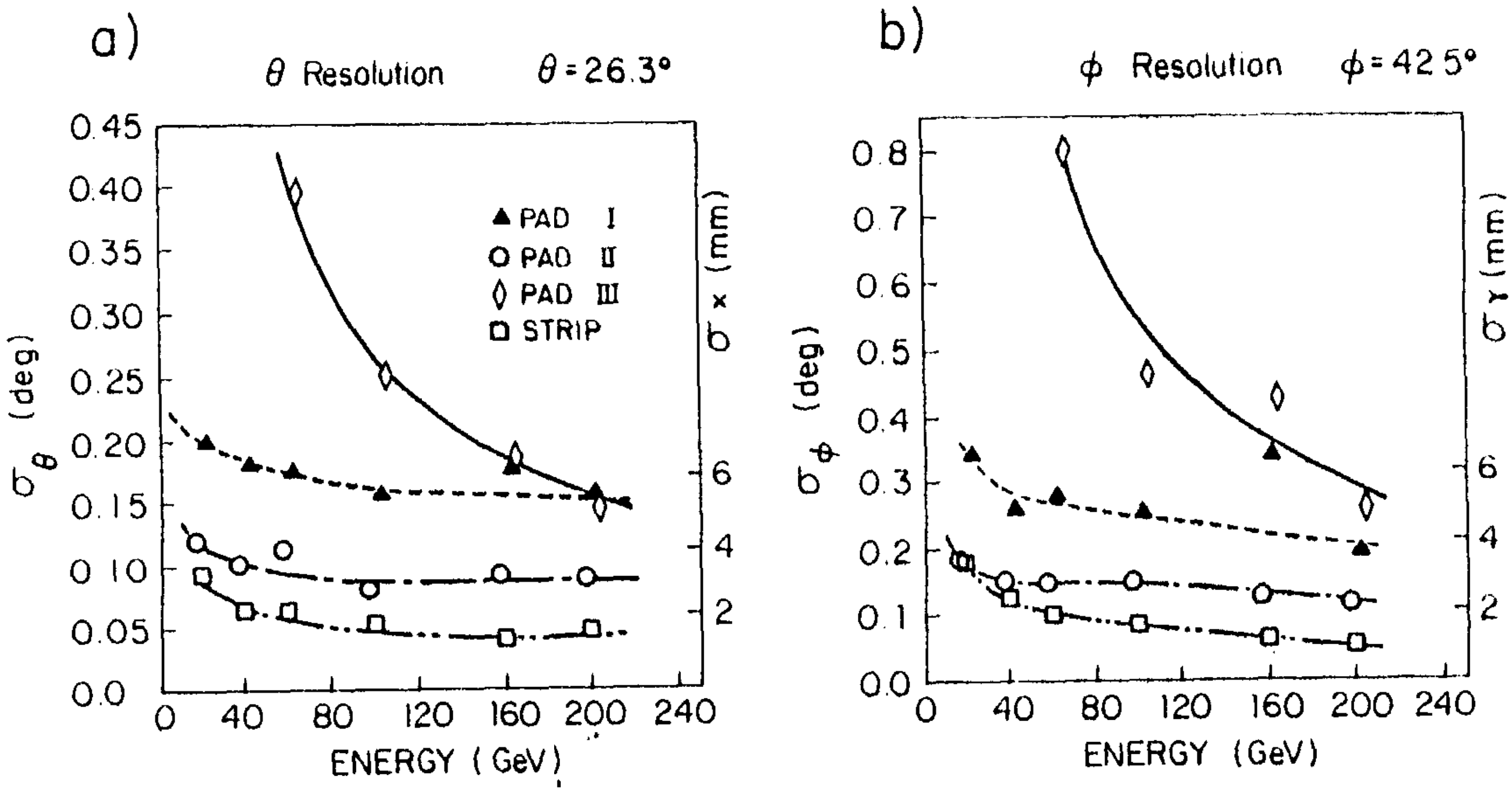

Fig 21

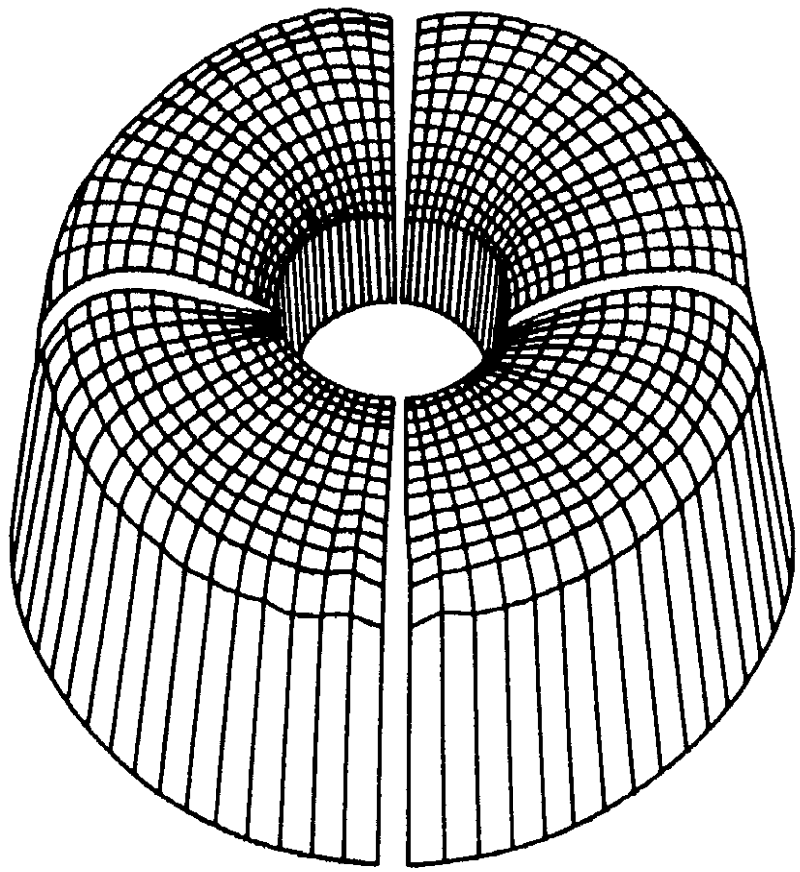

Fig. 22

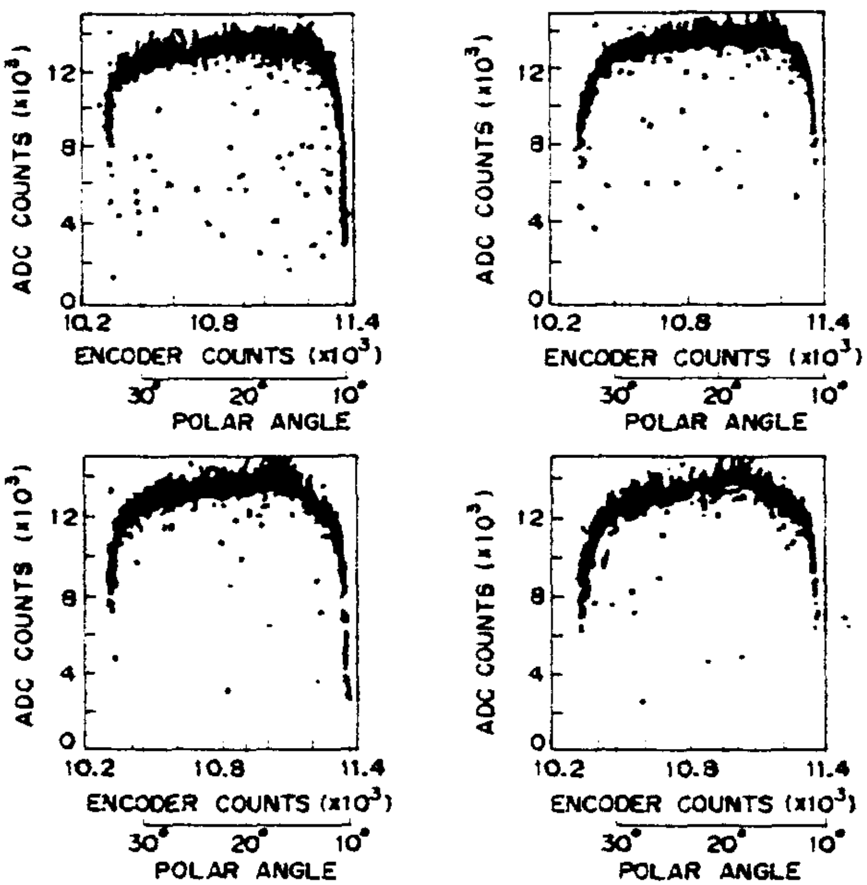

ADC COUNTS (x10³)
0
4
8
12
10.2
10.8
11.4
ENCODER COUNTS (x10³)
30°
20°
10°
POLAR ANGLE

Fig 23

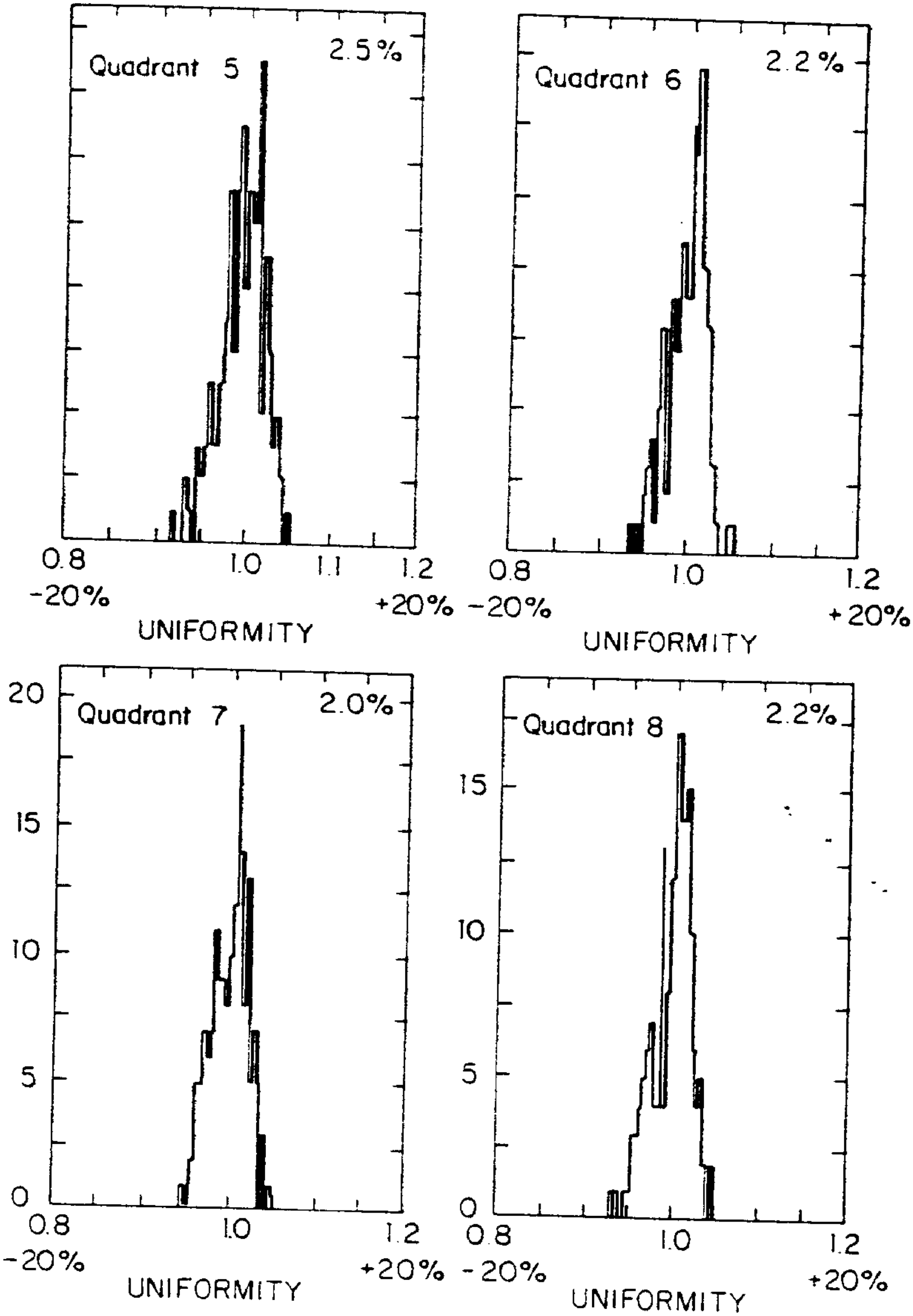

Quadrant 5
2.5%
0.8
-20%
1.0
1.1
1.2
+20%
UNIFORMITY
Quadrant 6
2.2%
0.8
-20%
1.0
1.2
+20%
UNIFORMITY
20
15
10
5
0
Quadrant 7
2.0%
0.8
-20%
1.0
1.2
+20%
UNIFORMITY
15
10
5
0
Quadrant 8
2.2%
0.8
-20%
1.0
1.2
+20%
UNIFORMITY

Fig 24

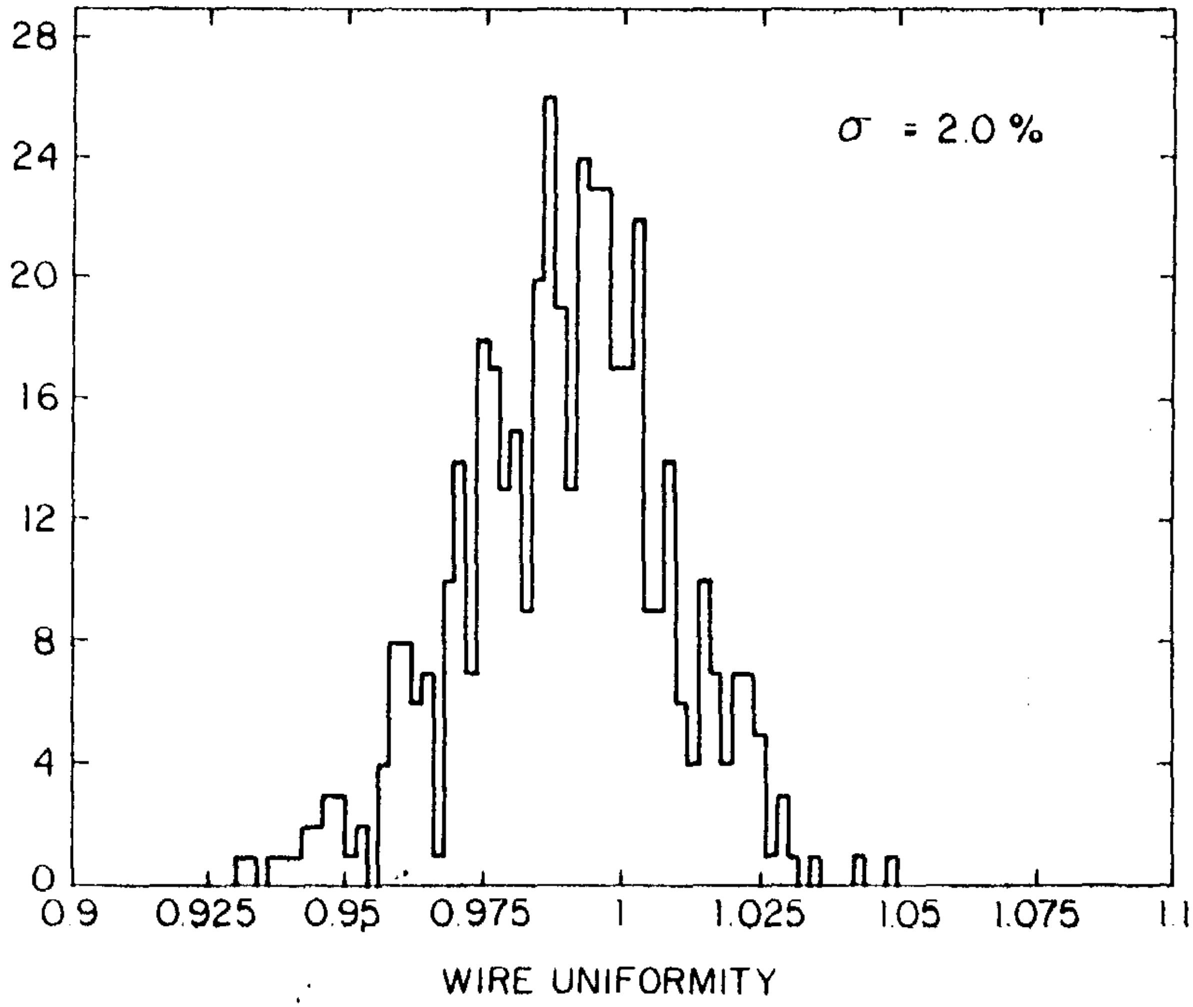
28
24
20
16
12
8
4
0
0.9
0.925
0.95
0.975
1
1.025
1.05
1.075
1.1
σ = 2.0 %
WIRE UNIFORMITY

Fig 25

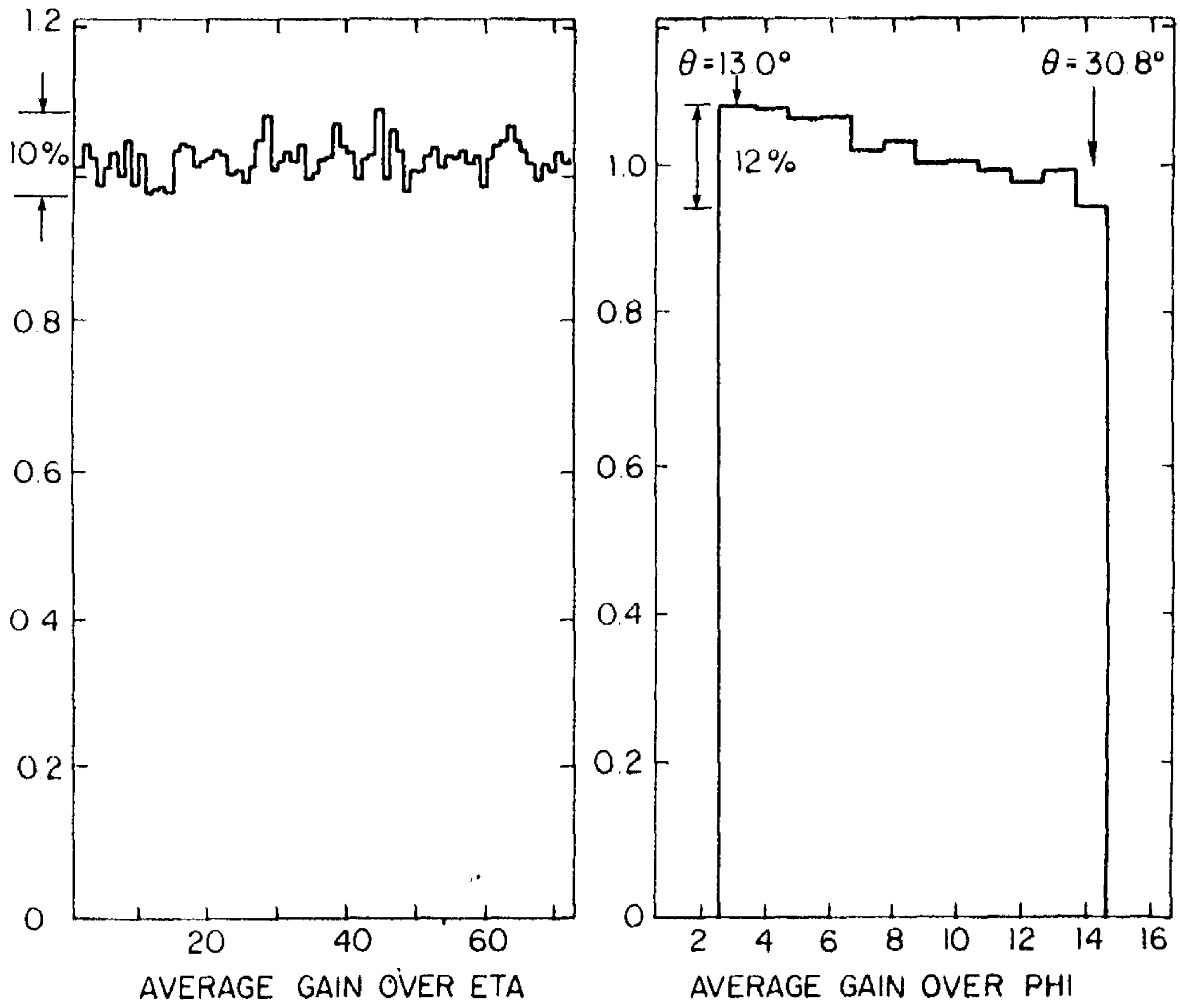
1.2
10%
0.8
0.6
0.4
0.2
0
20
40
60
AVERAGE GAIN OVER ETA
θ=13.0°
θ=30.8°
12%
1.0
0.8
0.6
0.4
0.2
0
2
4
6
8
10
12
14
16
AVERAGE GAIN OVER PHI

Fig 26a,b

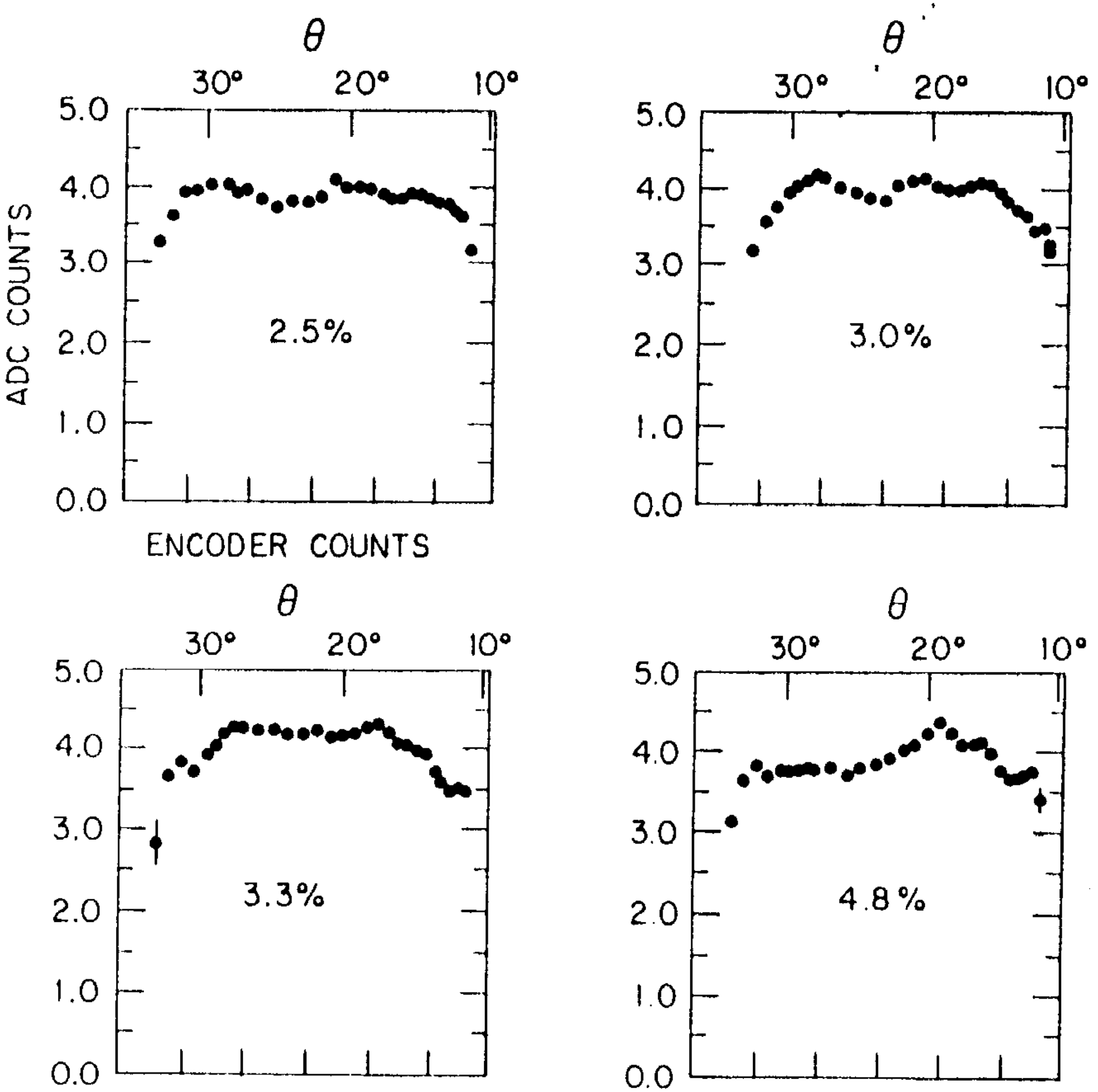

Uniformity of the Total Charge from Pad

fig 27a

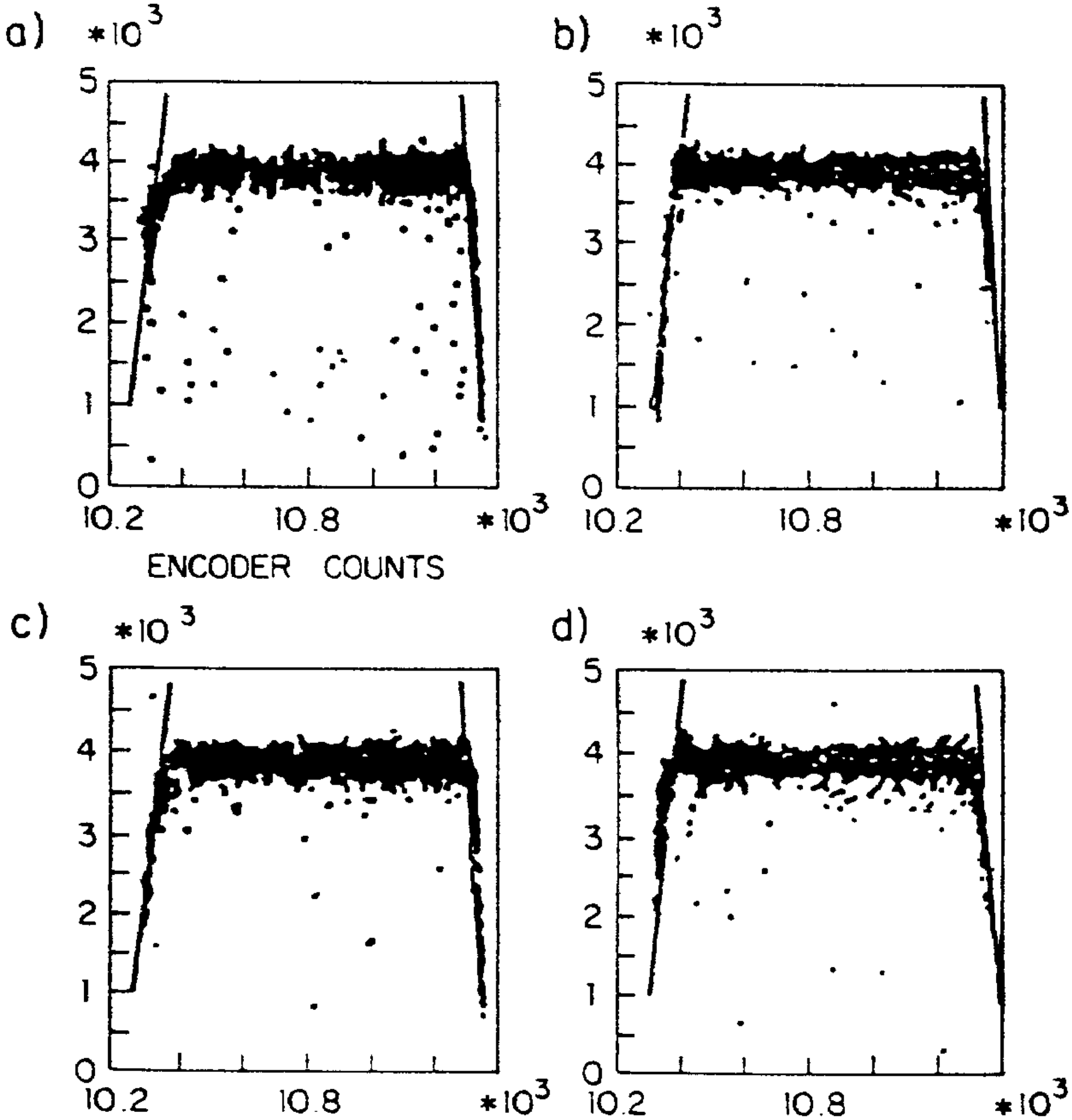
a)
*10^3
5
4
3
2
1
0
10.2
10.8
*10^3
ENCODER COUNTS
b)
*10^3
5
4
3
2
1
0
10.2
10.8
*10^3
c)
*10^3
5
4
3
2
1
0
10.2
10.8
*10^3
d)
*10^3
5
4
3
2
1
0
10.2
10.8
*10^3

Fig 27 b

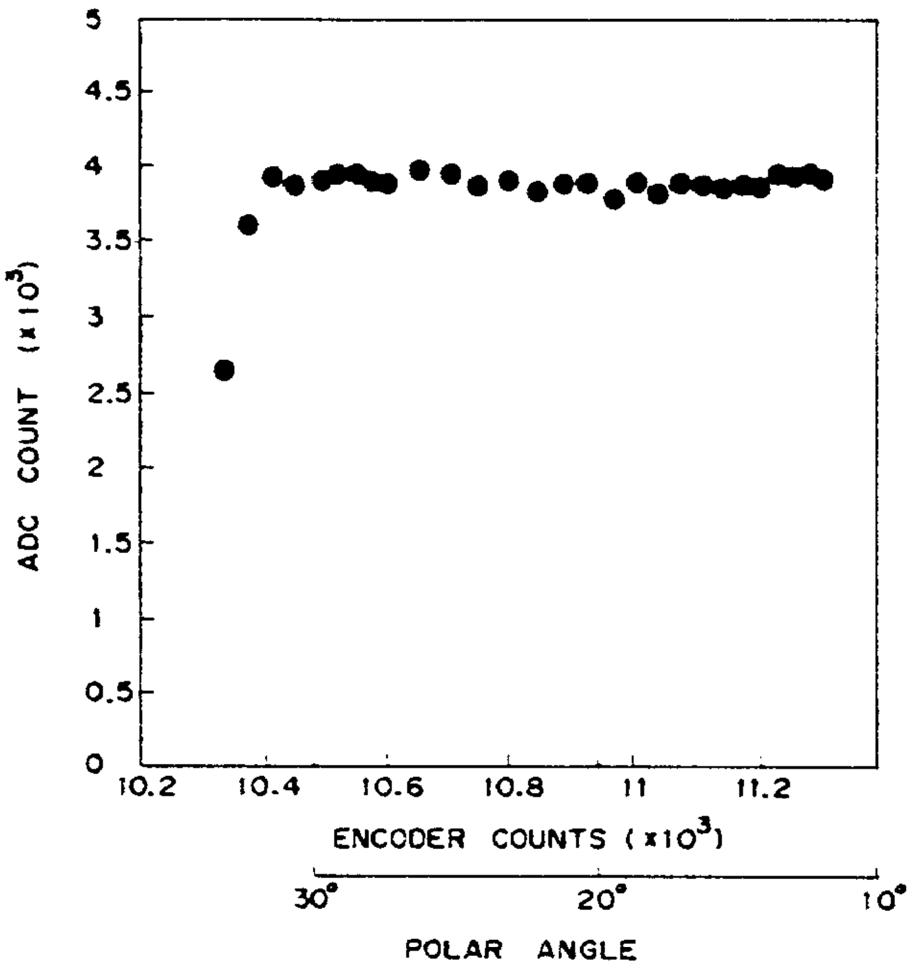

5
4.5
4
3.5
3
2.5
2
1.5
1
0.5
0
ADC COUNT (x10³)
10.2
10.4
10.6
10.8
11
11.2
ENCODER COUNTS (x10³)
30°
20°
10°
POLAR ANGLE

Fig 28

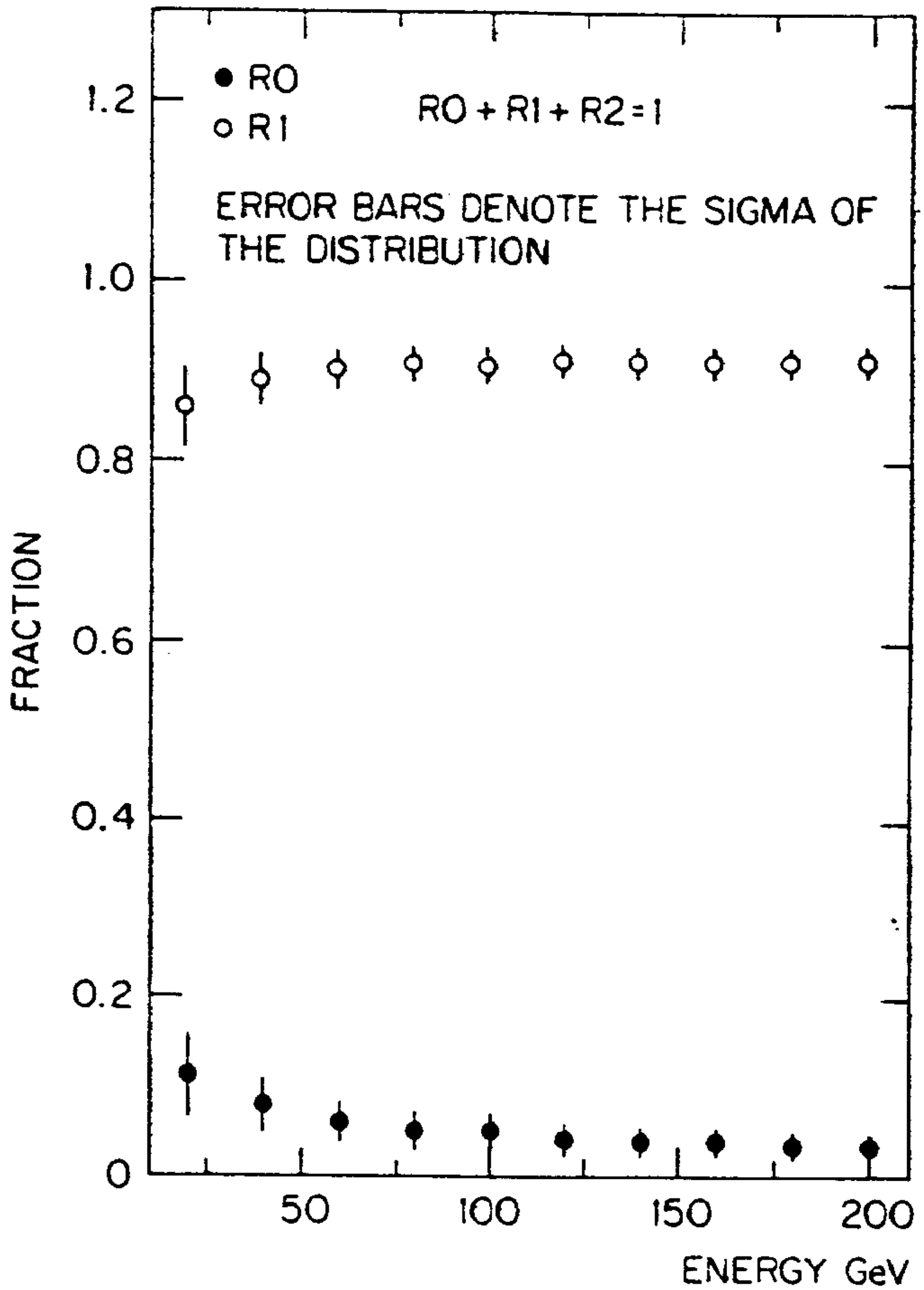

RO, R1 VS ENERGY

fig 29

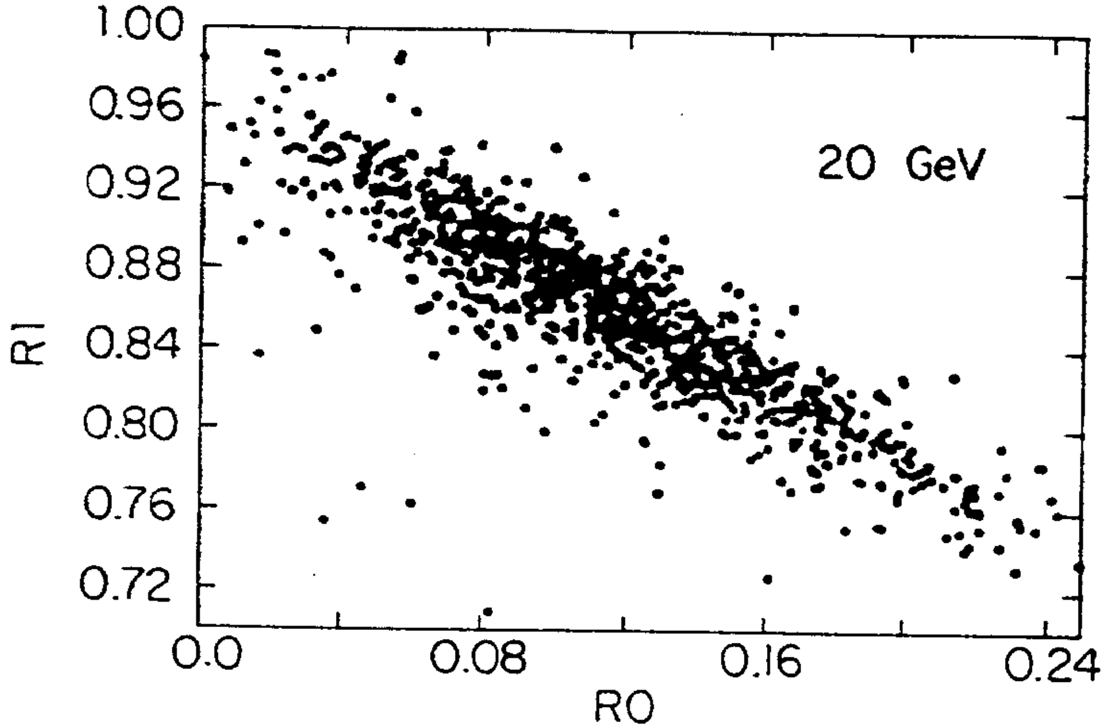

Fig 30a

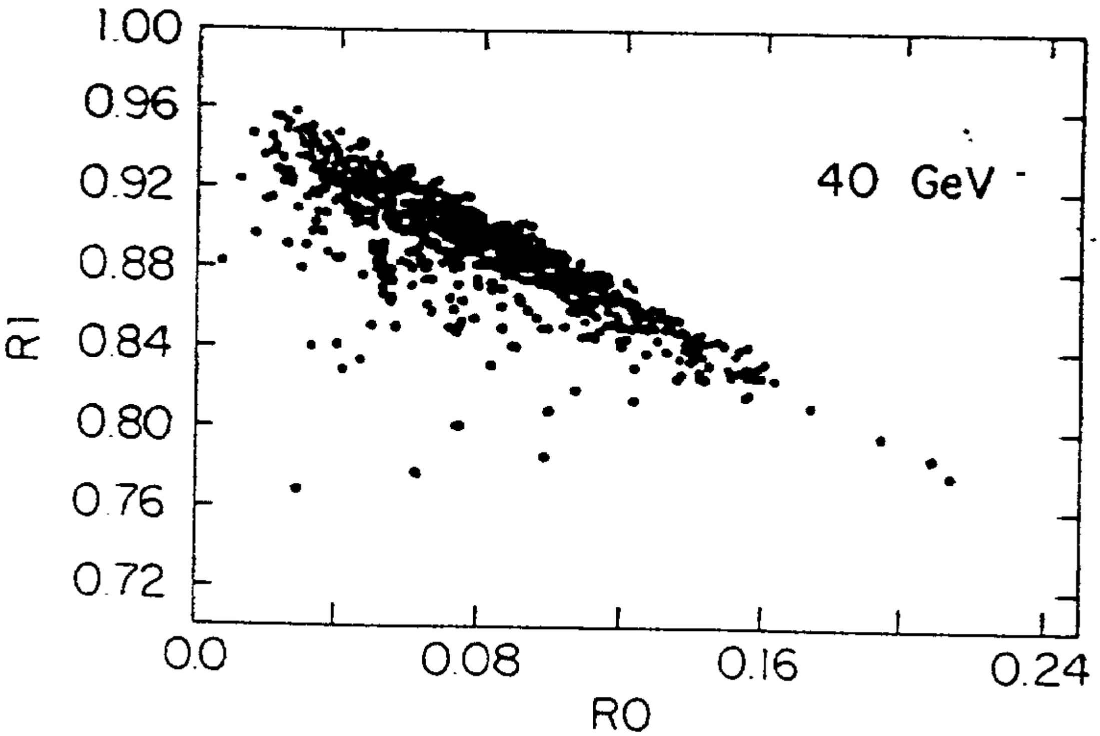

Fig 30b

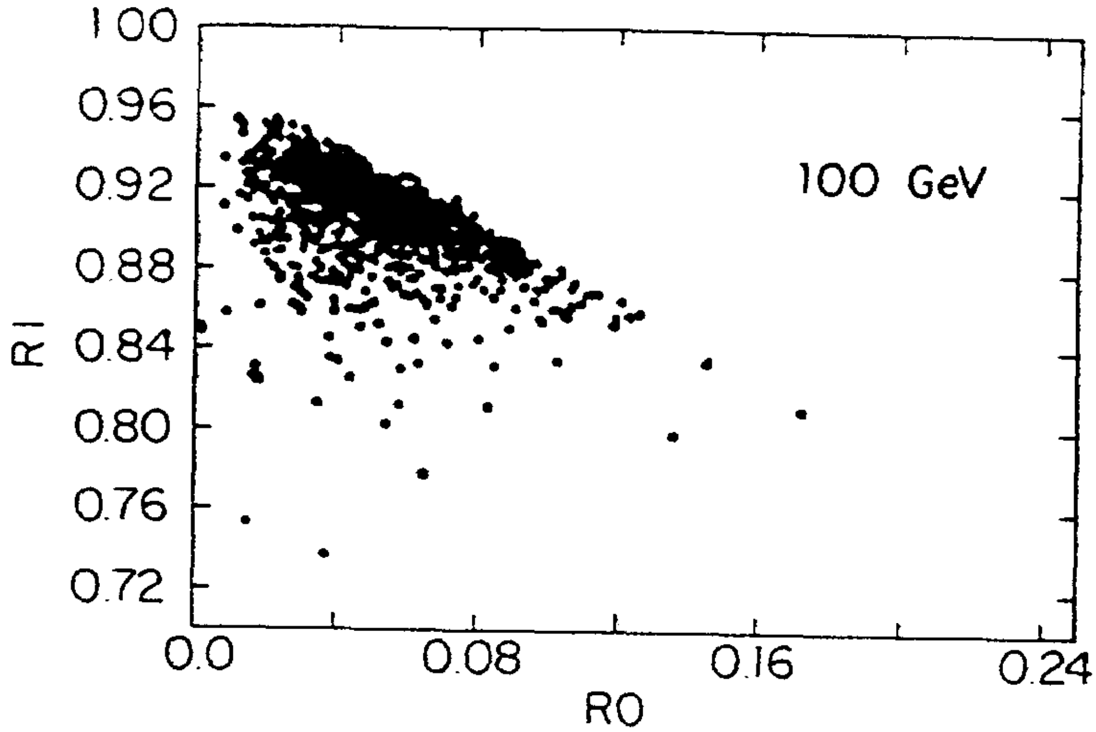

Fig 30c

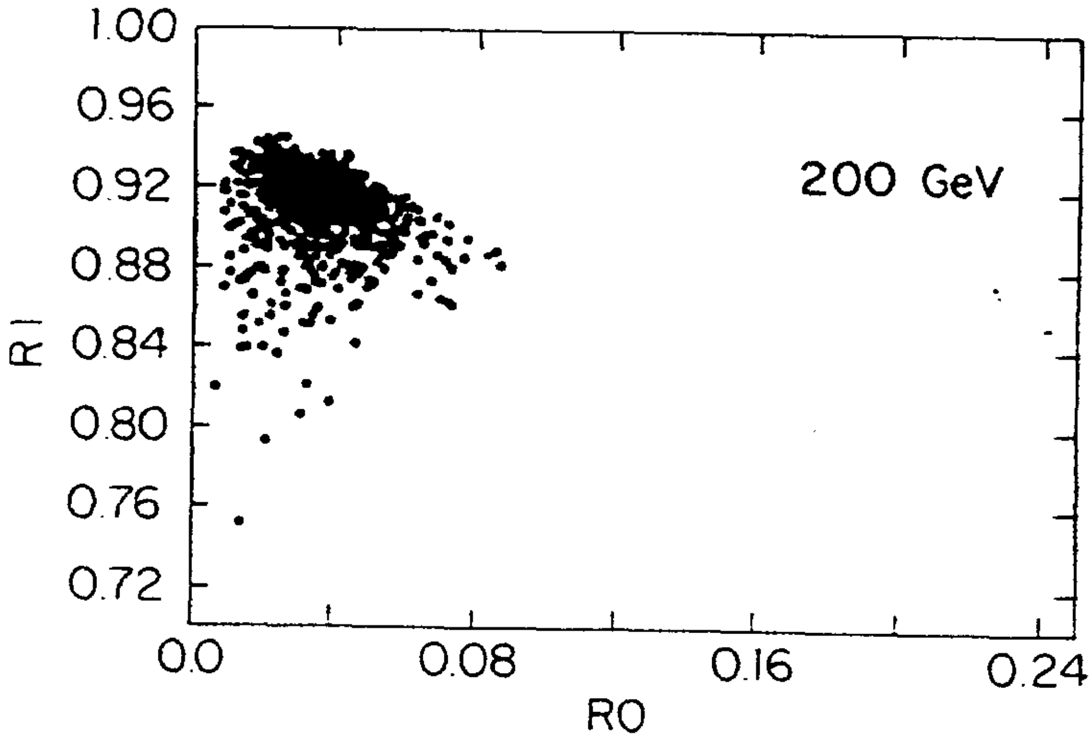

Fig 30d

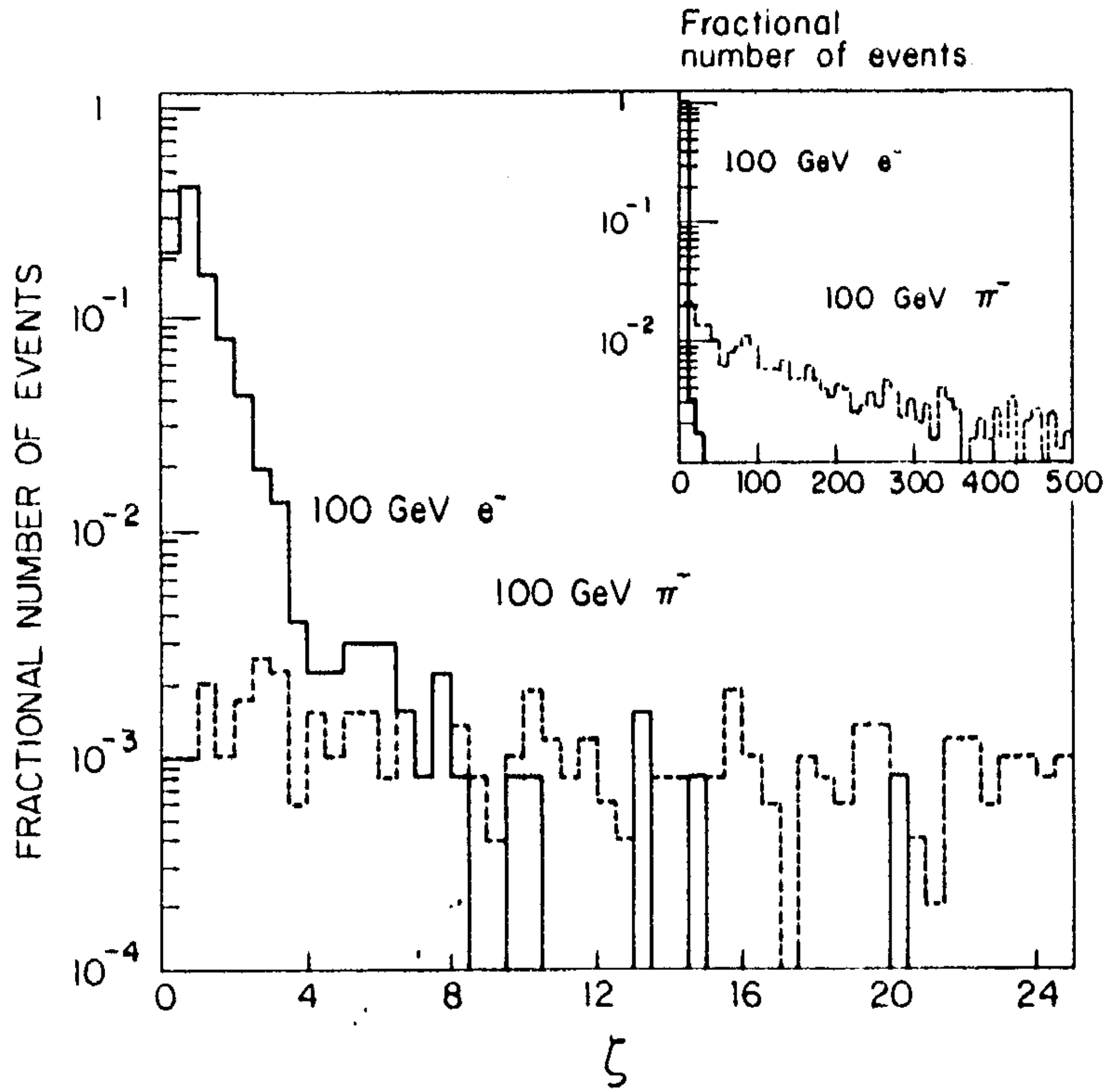
Fractional
number of events
100 GeV e⁻
100 GeV π⁻
10⁻¹
10⁻²
0 100 200 300 400 500
1
10⁻¹
10⁻²
10⁻³
10⁻⁴
FRACTIONAL NUMBER OF EVENTS
100 GeV e⁻
100 GeV π⁻
0 4 8 12 16 20 24
ζ

Fig. 31

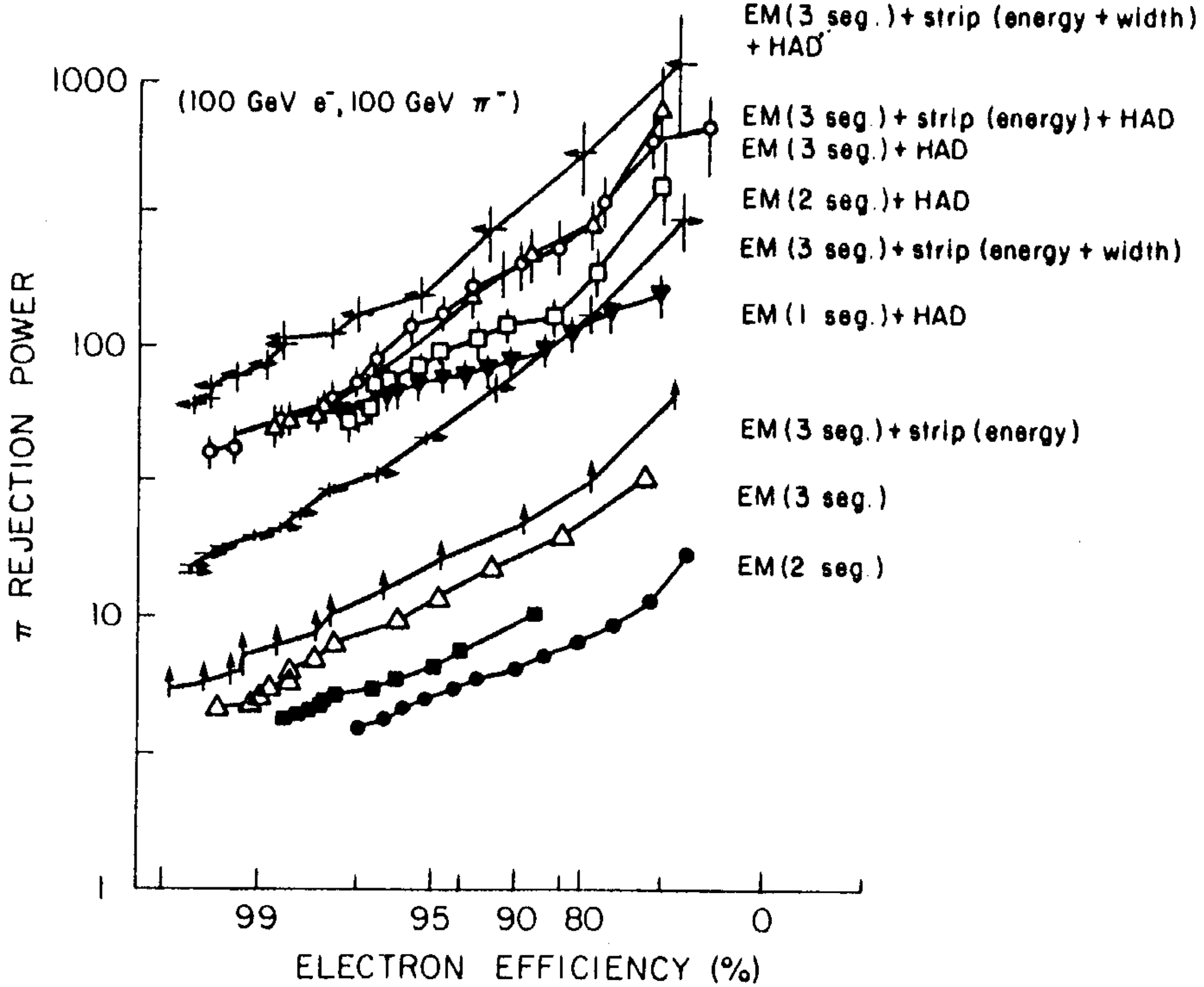
(100 GeV e⁻, 100 GeV π⁻)
π REJECTION POWER
1000
100
10
1
ELECTRON EFFICIENCY (%)
99
95
90
80
0
EM(3 seg.) + strip (energy + width) + HAD
EM(3 seg.) + strip (energy) + HAD
EM (3 seg.) + HAD
EM (2 seg.) + HAD
EM (3 seg.) + strip (energy + width)
EM (1 seg.) + HAD
EM (3 seg.) + strip (energy)
EM (3 seg.)
EM (2 seg.)

Fig. 32